Modeling surface water and groundwater mixing and mixing-dependent denitrification with bedform dynamics

Xue Ping[1], Zhang Wen[1,2*], Yang Xian[1], Menggui Jin[1,2], Stefan Krause[3]

[1]Hubei Key Laboratory of Yangtze Catchment Environmental Aquatic Science, School of Environmental Studies, China University of Geosciences, Wuhan, China

[2]State Key Laboratory of Biogeology and Environmental Geology, China University of Geosciences, Wuhan, China

[3]School of Geography, Earth and Environmental Sciences, University of Birmingham, UK

*Corresponding author: Zhang Wen (wenz@cug.edu.cn)

16   **Notation**

S Stream slope [-]

H Water depth [L]

U Stream velocity [L T^{-1}]

λ Ripple wavelength [L]

u_c Bedform migration celerity [L T^{-1}]

l Streambed height [L]

H_d Ripple height [L]

B Riverbed per unit width [L]

D_{50} Median sediment size [L]

x Horizontal coordinate, rightward positive [-]

y Vertical coordinate, upward positive [-]

k Sediment permeability [L^2]

K Sediment hydraulic conductivity [L T^{-1}]

h Hydraulic head [L]

h_m Amplitude of the sinusoidal head variation [L]

m Wavenumber of the variation [-]

g Gravity acceleration [L T^{-2}]

c_i Concentration of reactive components [M L^{-3}]

c_{gw} Groundwater tracer [M L^{-3}]

v Seepage velocity [L T^{-1}]

v_i Seepage velocity in the i-direction [L T^{-1}]

v_j	Seepage velocity in the j-direction [L T^{-1}]
θ	Sediment porosity [-]
α_L	Longitudinal dispersivity [L]
α_T	Transverse dispersivity [L]
D_{ij}	Hydrodynamic dispersion [L^2 T^{-1}]
D_m	Molecular diffusion coefficient [L^2 T^{-1}]
ι	Tortuosity factor [-]
V_{AR}	Maximum reaction rate of aerobic respiration [T^{-1}]
V_{DN}	Maximum reaction rate of denitrification [T^{-1}]
K_{inh}	Non-competitive inhibition factor [M L^{-3}]
K_{DOC}	Half-saturation for dissolved organic carbon [M L^{-3}]
K_{NO3^-}	Half-saturation for nitrate [M L^{-3}]
K_{O2}	Half-saturation for oxygen [M L^{-3}]
X_{AR}	Microbial concentration facilitating aerobic respiration [M L^{-3}]
X_{DN}	Microbial concentration facilitating denitrification [M L^{-3}]
ρ_s	Sediment density [M L^{-3}]
ρ	Water density [M L^{-3}]
P	Hydraulic pressure [M L^{-1}T^{-2}]
D^*	Dimensionless particle parameter [-]
u^*	Bed shear velocity [L T^{-1}]
u_{cr}^*	Critical bed shear velocity [L T^{-1}]
n	Manning coefficient [-]

τ^*	Shield parameter [-]
τ_{cr}	Critical shear stress [M L^{-1}T^{-2}]
τ_{cr}^*	Critical Shield parameter [-]
r	Submerged specific gravity of sediment [-]
R_{O2}	Aerobic respiration rate [M L^{-3}T^{-1}]
R_{s-NO3}	Non-mixing-dependent denitrification rate [M L^{-3}T^{-1}]
R_{g-NO3}	Mixing-dependent denitrification rate [M L^{-3}T^{-1}]
R_{DOC}	Dissolved oxygen carbon consumption rate [M L^{-3}T^{-1}]
υ	Kinematic viscosity of water [L^2 T^{-1}]
μ	Dynamic viscosity of water [M L^{-1} T^{-1}]
u_s	Underflow seepage velocity induced by stream gradient [L T^{-1}]
Re	Reynolds number [-]
U_r	ratio of bedform celerity to pore water velocity [-]
u_p	Darcy velocity induced by pumping process [L T^{-1}]
u_q	Vertical groundwater flux [L T^{-1}]
U_b	Ratio of vertical groundwater flux to hyporheic exchange flux
τ_R	Biogeochemical reaction timescale [T]
τ_T	Water transport timescale [T]
Da	Damköhler number [-]
Δx	Bedform migrating displacement per timestep (L)
dt	The length of per timestep (T)
Da'	Conversion factor for unit Darcy to m^2 [-]

F_{mix} Proportion of mixing flux to hyporheic exchange flux [-]

A_{mix} Proportion of mixing zone to the whole domain [-]

A Streambed area [L^2]

M_{NDN} Nitrate removed by non-mixing-dependent denitrification [$M\ T^{-1}$]

M_{DN} Nitrate removed by mixing-dependent denitrification [$M\ T^{-1}$]

N_{RE} Nitrate removal efficiency [-]

M_{in} Nitrate being introduced into streambed [$M\ T^{-1}$]

Fin Oxygen influx [$M\ L^{-2}\ T^{-1}$]

$Fout$ Oxygen outflux [$M\ L^{-2}\ T^{-1}$]

Ao Oxygenated area [L^2]

Abbreviations

HZ   Hyporheic zone

SW   Surface water

GW   Groundwater

HEF   Hyporheic exchange flow

MF   Mixing flux

NMD   Non-mixing-dependent

MD   Mixing-dependent

AR   Aerobic respiration

DN   Denitrification

RMSE   Root means square error

DNRA   Dissimilatory nitrate reduction to ammonium

ANAMMOX Anaerobic ammonium oxidation

17

Abstract The hyporheic zone (HZ), where surface water (SW) and groundwater (GW) interact and mix, acts as a critical interface that attenuates contaminants through enhanced biogeochemical cycling. While bedform migration significantly influences hyporheic exchange and non-mixing-driven reactions of solutes from upstream SW, the effects of bedform migration on SW-GW mixing dynamics and mixing-triggered biogeochemical reactions—particularly under gaining stream conditions—remain poorly understood. Establishing~~Pioneering~~ a coupled hydrodynamic and reactive transport model that incorporates bedform migration, this paper systematically examines nitrogen processing for scenarios of variable sediment grain size, stream velocities, and upwelling GW fluxes. Results of this study reveal that SW-GW mixing and mixing-triggered denitrification zones progressively transition from crescent shapes into uniform band-like configurations as bedforms migrate. Both hyporheic exchange flux and mixing flux increase with increasing stream velocity and associated bedform celerity. The mixing proportion and mixing zone size increase at the start of migration, while they reach~~remain~~ approximately stable ~~constant~~ when turnover becomes the dominant hyporheic water~~ ~~exchange mechanism ~~for fine-medium sandy riverbed~~. Slow to moderate migrated bedforms with enhanced mixing dynamics facilitate mixing-triggered denitrification, whereas fF̶ast stream flows and migrating bedforms shorten ~~reduce~~ solute residence timescales and limits denitrification potential~~opportunities~~. Consequently, in fine to medium sandy sediments, groundwater-borne nitrate removal efficiency declines significantly with bedform migration. ~~Consequently, nitrate removal efficiency from both stream- and groundwater-borne sources decreases significantly with bedform migration in fine-medium sandy sediments.~~ The self-purification capacity of the HZ, and particularly its functioning as a natural barrier against GW

40 contamination, is hindered under such dynamic bedform conditions. These findings highlight the

41 need to maintain stable bedform conditions in restoration projects to enhance the capacity of HZ

42 contaminant attenuation.

1. Introduction

44   Anthropogenic activities such as the intensification of agricultural practices with its

45 increased used of mineral and organic fertilizers, together with high livestock densities and

46 emissions of inadequately treated domestic and industrial wastewater have significantly

47 increased nitrogen loading to rivers and groundwater, which impacts water quality, causing

48 eutrophication, hypoxic and related deterioration of ecosystem functions (Conley et al., 2009;

49 Rouse et al., 1999). Long-term regulatory monitoring data (e.g., from the UK) indicate that

50 nitrate levels have stabilized in many rivers, while nitrate concentrations in groundwater-fed

51 rivers continue to increase (Burt et al., 2011; Howden and Burt, 2008). The persistence of nitrate

52 contamination in groundwater and associated risks of a "nitrate time bomb" (Ascott et al., 2019)

53 has highlighted the urgency of exploring the potential of natural microbial processes to mediate

54 nitrate transformation and removal in riverbed sediments (Shelley et al., 2017; Lansdown et al.,

55 2015; Rivett et al., 2008).

56   The hyporheic zone (HZ) has received significant attention for its potential to facilitate

57 enhanced nitrate transformation and removal via denitrification that is a primary process

58 permanently reducing nitrate, with hyporheic exchange flows (HEFs) acting as a critical

59 mechanism for transporting nitrate-rich surface water to the riverbed sediments where microbial

60 activities and biogeochemical reaction rates are enhanced (Boano et al., 2014; Boulton et al.,

61 1998; Cardenas, 2015; Xian et al., 2022; Krause et al., 2022). It has for long been assumed that

62 predominantly stream waters provide inputs of bioavailable (mainly dissolved) organic carbon

63 (DOC), oxygen (O_2) and nitrate (NO_3 ~~NO_3~~) into the riverbed where the residence and reaction

64 times determine the occurrence of aerobic respiration and the potential for shifts into anaerobic

65 conditions that may facilitate denitrification along the HEF paths in the presence of enough

66 remaining DOC (Zarnetske et al., 2011a, b). These hydrological and biogeochemical

67 mechanisms are in this form mainly representative of headwater streams, where the HEF is

68 induced by stream flow turbulence (Boano et al., 2011; Roche et al., 2018, 2019), local

69 geomorphological setting (Cardenas et al., 2008; Marzadri et al., 2012; Tonina and Buffington,

70 2007), and flow obstacles such as woody debris, streambed engineering or restoration structures

71 (Briggs et al., 2013; Wondzell et al., 2009), and hyporheic nitrate removal processes expected to

72 mainly occur at the middle to end- hyporheic flow paths within HEF cell sediments.

73   In lowland systems, groundwater-fed streams and rivers in permeable catchments will be

74 dominated by base flow of often nitrate enriched groundwaters. The subsurface hydrological

75 conditions are driven by horizontal HEF as well as vertical fluxes resulting from regional

76 groundwater flow toward (or from) the stream. Spatial variability in regional groundwater flow

77 can significantly affect hyporheic exchange and biogeochemical cycling (Boano et al., 2013;

78 Krause et al., 2013; Munz et al., 2011; Naranjo et al., 2015). It is important to note that the

79 groundwaters of many piedmont plains and lowlands are often contaminated with high nitrate

80 concentrations, but usually low in bio-available DOC (Krause et al., 2022). When nitrate-rich

81 groundwater upwells through deeper sediments and reaches a region enriched in availability of

82 DOC, nitrate reduction processes are significantly facilitated in the condition (Krause et al.,

2009; Naranjo et al., 2015; Ping et al., 2023; Trauth et al., 2017). Stelzer and Bartsch (2012)

developed such a conceptual framework of nitrate-rich gaining fluvial setting from 8 sites in the

Waupaca River Watershed with three order magnitude in groundwater nitrate concentration.

Lansdown et al. (2014) also measured high denitrification rate at deep sediment in the coarse-

grained sediments typical of groundwater-fed system, located within the River Leith (Cumbria,

UK) where diverse nitrogen concentration changes were confirmed earlier (Krause et al., 2009).

Turnover and removal of the large amounts of NO_3^- from groundwater require DOC either

from autochthonous streambed sources or from downwelling surface water to stimulate nitrate

reduction (Krause et al., 2013, 2022; Ping et al., 2023; Sawyer, 2015; Trauth et al., 2017). For

coarse grain or sandy riverbeds with low autochthonous organic matter content, stream-borne

DOC dominates the supply of carbon sources for nitrogen transformation processes. Sandy

sediments with less autochthonous organic carbon sources covering the majority of alluvial

riverbeds are commonly characterized by topographical features such as ripples, dunes, and

riffle-pool sequenced. The typical and multiple HEF cells induced by bedform topography are

generally in crescent shapes (Fox et al., 2014; Wu et al., 2024). The downward advection of

stream borne DOC provides electron donor and mixes with nitrate-rich and anoxic groundwater.

It has been shown that the highest potential for mixing triggered denitrification is often found at

the margin of the HEF cells, which represents the last natural protection before nitrate enter a

stream (Hester et al., 2013, 2014; Gu et al., 2008; Nogueira et al., 2022).

The effects of mixing triggered denitrification on groundwater borne nitrate transformation

in HZs have been studied almost exclusively for the case of stationary, that is immobile

bedforms (Hester et al., 2017, 2019; Trauth and Fleckenstein et al., 2017; Ping et al., 2023).

Bedforms are mobile in dynamic equilibrium or undergo constant changes during periods of moderate to high stream flow, and they are typically found in medium and larger waterways under realistic field conditions (Bartholdy et al., 2015; Risse-Buhl et al., 2023; Schindler et al., 2015). For example, Harvey et al. (2012) observed the migrating bedforms of dunes (with a median grain size D_{50} of 380 μm for the riverbed sediments) at a velocity of 57.6 cm/h during base flow in the "Clear Run" stream in eastern North Carolina, USA. Ahmerkamp et al. (2017) found that the ripple bedforms for sands (D_{50} = 63 μm) ranged from 11 to 29 cm with a constant ratio of bedform height and length at 1/9, and migrated at velocities of 0.7–6.5 cm/h in the German Bight, Southeastern part of the North Sea. Bedforms migration complicates the development of hyporheic flow fields, facilitateincreases solute exchange, alters redox conditions in riverbeds, and affects contaminant transport and transformation (Ahmerkamp et al., 2015; Schulz et al., 2023; Peleg et al., 2024). Previous studies focused on ripple-driven hyporheic exchange in headwater to midstream reaches under neutral conditions, and simulated bedform migration via a moving frame of reference (Ahmerkamp et al., 2015; Jiang et al., 2022; Kessler et al., 2015; Ping et al., 2022;Zheng et al., 2019). Ping et al. (2022) used a fixed reference frame and noted that bedform migration negatively impacts non-mixing-dependent denitrification rates and stream-borne nitrate removal efficiencySpecifically, bedform migration has negative influences on non-mixing-dependent denitrification (where nitrate and DOC are both derived from surface water and travel together along the flow paths) rate and nitrate removal efficiency (Jiang et al., 2022; Kessler et al., 2015; Ping et al., 2022; Zheng et al., 2019). However, no studies have yet investigated the effects of bedform migration on surface water-groundwater mixing in the lowland reaches of streams under gaining conditions, nor have they

explored its controls or implications for mixing-induced denitrification in groundwater-fed streams and rivers. However, no studies have yet investigated and explored the effects of bedforms migration on mixing of surface water and groundwater, as well as its controls and implications for mixing triggered denitrification reaction in groundwater-fed streams and rivers.

In this study, numerical modeling of hyporheic flow and multi-component solute (DOC, O_2, and NO_3^-) transport is used to evaluate study the effect of bedform migration on mixing-dependent denitrification in the HZ of a gaining river, where the overlying stream water is induced into the sediment by ripple-type bedforms. The objectives of this study are to determine the effects of bedform migration on the overall extent and magnitude of mixing of surface water and upwelling groundwater, as well as its influences on groundwater-borne nitrate transport and transformation.

2. Methods

2.1 Model description

SThe stream flow over the bedform generates head gradients along the riverbed surface, drives hyporheic exchange, and induces the formation of periodic ripples. Hyporheic flow, solute transport, and biogeochemical reactions were modelled in saturated sediments beneath a riverbed. Ripples develop form in the riverbed and migrate downstream above the riverbed surface as a consequence ofdue to sediment bedload transport processes, with sediment grain eroded and deposited at the surface., whereas deeper streambed sediments remain relatively stable (Harvey et al., 2012; Precht et al., 2004). From the perspective of an observer who stands at the target single riverbed and watches the ripples passing by, the bedform shapes and

associated pressure profiles migrate downstream over the immobile riverbed layer. Because

ripple heights (H_d = 2 cm) accounts for 20% of the stream water depth (H = 10 cm) and are far

smaller than that of the underlying immobile domain (l = 16 cm), the undulating riverbed can be

reasonably approximated as a flat bed with time-varying pressure patterns during bedform

migration. Besides, reactive solute transport also primarily takes places within the immobile

riverbed sediment. Therefore, a two-dimensional (2D) rectangular domain is constructed with a

length (λ) of 0.2 m and depth (l) of 0.16 m. A fixed reference frame is adopted, with its origin

located at the bottom-left corner of the model. Here, the horizontal direction corresponds to the

x-axis and the vertical direction to the y-axis. The model domain has four corners: A (0, 0), B (0,

l), C (λ, l), and D (λ, 0). The lateral boundaries are AB (left, x = 0) and CD (right, x = λ); the top

boundary is BC (y = l), and the bottom boundary is AD (y = 0).

    The model schematic is sketched in Figure 1. The model is relevant to the model used by

Ping et al. (2022) but with significant differences. Specifically, Ping et al. (2022) focused on

ripple-driven hyporheic exchange processes in the headwater to midstream sections of streams

under neutral conditions. In contrast, the present study focuses on the downstream sections of

rivers under gaining conditions, aiming to simulate surface water-groundwater interacting and

mixing processes under dynamic bedforms. To our knowledge, previous migrating ripple models

have extensively examined surface water-groundwater interaction processes (i.e., ripple-driven

hyporheic exchange processes), yet the mixing process remains uninvestigated (Ahmerkamp et

al., 2017; Jiang et al., 2022; Zheng et al., 2019; Kessler et al., 2015). In downstream sections,

groundwater is typically nitrate-contaminated, and denitrification is often co-regulated by both

mixing regimes. The model is also developed with advancements of these previous models by

including an important biogeochemical reaction in nitrate dynamics, that is mixing-triggered

171 denitrification (see next section for details).

Head imposed along top boundary at t_0 and t_1
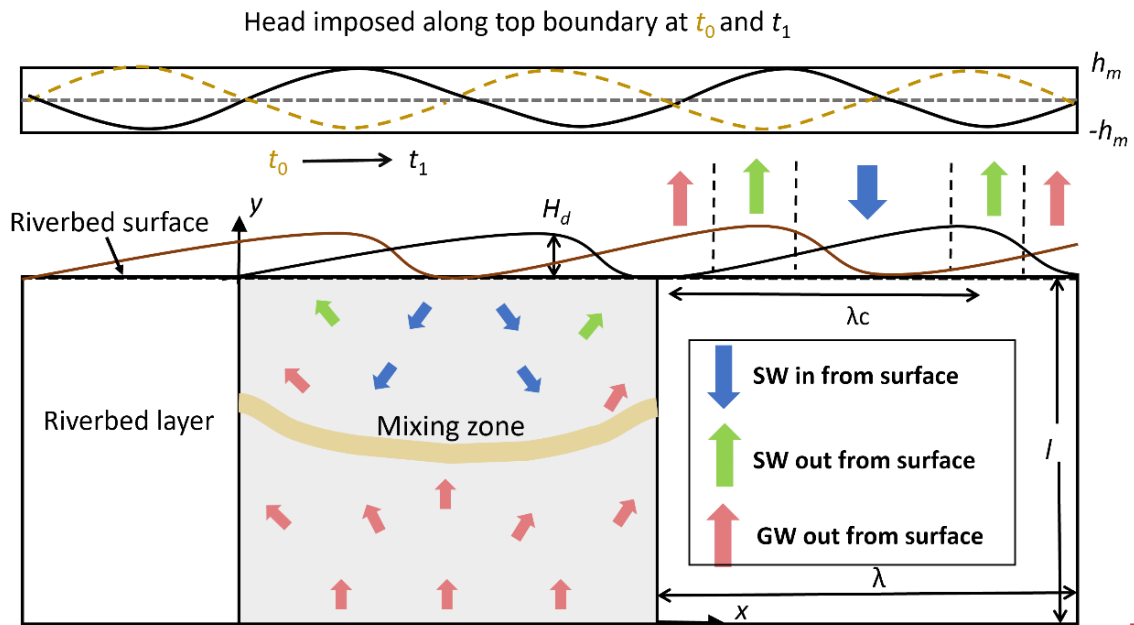
172 The

173 stream geometry is parameterized through its slope S, average water depth H, and mean velocity

174 U. Triangular shaped ripple bedforms of wavelength λ are considered to develop and migrate

175 downstream by a unidirectional average velocity u_c. Flow is driven by pumping (pressure

176 variation along the bedform surface) and bedform migration processes and influenced by

177 upwelling groundwater.
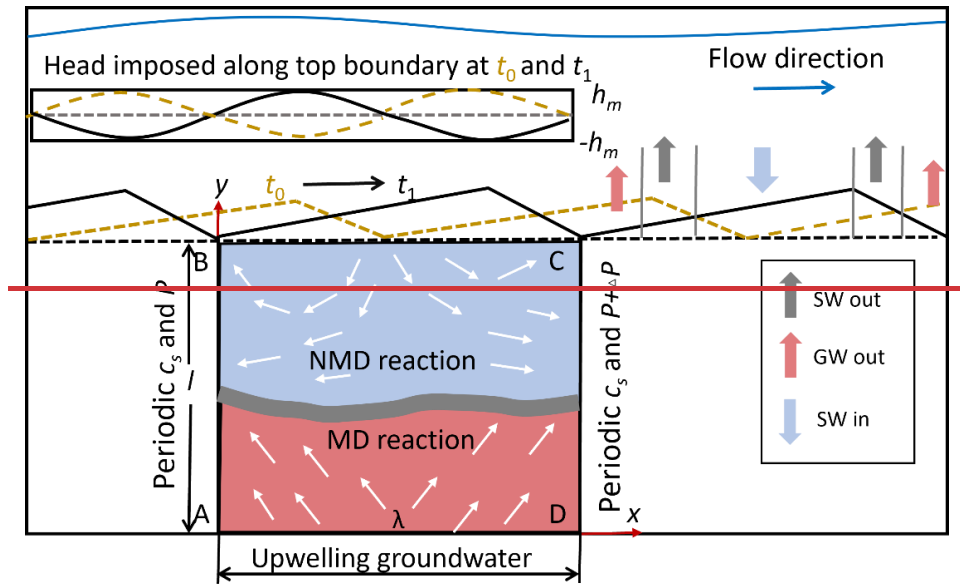
Figure 1. Schematic of the model domain with bed form geometry ~~and boundary conditions~~.

Stream flow and bedform migration are from left to right. The dashed yellow lines represent the streambed surface and head profile at time t_0, and the solid black lines represent the streambed surface and head profile after migration at t_1. "SW in" is where surface water enters the riverbed layer, ~~and~~ "SW out" is where surface water discharges to the stream, and "GW out" is along the upstream and downstream sides of bedforms where groundwater discharges to the stream. The yellow~~gray~~ band represents the mixing zone of surface water and groundwater. NMD reaction = non-mixing-dependent reaction and MD reaction = mixing-dependent reaction. This figure is modified from Figure 2 in Ping et al. (2022), with permission granted by Wiley.

In this study, hyporheic flow, multi-component solutes (DOC, O_2, and NO_3^-) transport, and biogeochemical reactions (both non-mixing-dependent NMD and mixing-dependent MD reactions) are modelled in saturated sediments beneath a riverbed layer. Stream flow over the riverbed is not simulated. The hyporheic exchange flow is driven by pumping (overlying flow over the bed form produces a hydraulic head $h|_{y=l}$) and bedform migration (triangular shaped

ripples migrate downstream by an average velocity u_c) and influenced by upwelling

groundwater. Stream water transports DOC, O_2, and NO_3^- into the riverbed, whereas

groundwater polluted with NO_3^- upwells toward the stream. In order to distinguish NMD and

MD denitrification, we define stream-borne nitrate (s-NO_3^-) and groundwater-borne nitrate (g-

NO_3^-) as two distinct reactants.

2.2 Model formulation

2.2.1 Governing equation

The pore water flow was calculated using Darcy's law and the groundwater flow equation:

$$\nabla \cdot \left(-K\nabla h \right) = 0 \tag{1}$$

where h [L] is the hydraulic head, and K [L T^{-1}] $= k\rho g/\mu$ is the hydraulic conductivity, k [L^2] is

the permeability of the riverbed, ρ [M L^{-3}] are the density of water, g [L T^{-2}] is the gravity

acceleration, and μ [M L^{-1} T^{-1}] is the dynamic viscosity of water.

The head profile on the streambed surface (BC) was described as a sinusoidal function that

moves downstream by the ripple's migration velocity u_c (Ping et al., 2022):

$$h\big|_{y=l} = h_m \cdot \sin m(x - u_c dt) \tag{2}$$

where h_m [L] is the amplitude of the head variation, m [ ] is the wave number of the variation (m

$= 2\pi/\lambda$), the head difference is related to the properties of the overlying flow (Elliott and Brooks,

1997):

$$h_m = a \frac{U^2}{2g} \left(\frac{H_d / H}{0.34} \right)^m \tag{3}$$

212 ~~where *a* = 0.28 [-] is a dimensionless coefficient, U [L T^{-1}] is the average stream velocity, H_d [L]~~

213 ~~is the height of the ripple, H [L] is the water depth, and g [L T^{-2}] is the gravity acceleration. The~~

214 ~~exponent *n* equals to 3/8 if H_d < 0.34H and 3/2 otherwise.~~

215   The transport of reactive solutes within the streambed sediment was described by the

216 advection-dispersion-reaction equation:

$$\frac{\partial c_i}{\partial t} - \nabla \cdot \left(D_{ij} \nabla c_i \right) + \nabla \boldsymbol{v} c_i = R_i \tag{24}$$

218 where c_i [M L^{-3}] represents the concentration of reactive components, $\boldsymbol{v}$ [L T^{-1}] is the seepage or

219 linear pore water velocity <u>vector</u>, <u>D_{ij} [L^2 T^{-1}] is the hydrodynamic dispersion tensor, and R_i [M</u>

220 <u>L^{-3}T^{-1}] denotes the biogeochemical rate of reactive components; the elements of the dispersion</u>

221 <u>tensor D_{ij}</u> ~~[L^2 T^{-1}]~~ <u>are</u>~~is the hydrodynamic dispersion~~ <u>and is</u> defined by Bear and Verruijt

222 (1998):

$$D_{ij} = \left(\alpha_L - \alpha_T \right) \cdot \frac{v_i v_j}{|\boldsymbol{v}|} + \delta_{ij} \cdot \left(\alpha_T |\boldsymbol{v}| + \theta \cdot \iota D_m \right) \tag{53}$$

224 where α_L [L] and α_T [L] are longitudinal and transverse dispersivities, respectively, D_m [L^2 T^{-1}] is

225 molecular diffusion coefficient<u>, v_i and v_j denote the seepage velocities in the *i*-direction and *j*-</u>

226 <u>direction, respectively;</u> and ι [-] is tortuosity.

227   ~~The reactive transport model considered three chemical species: DOC, O$_2$, and NO$_3$$^=$. In~~

228 ~~order to distinguish non-mixing-dependent and mixing-dependent denitrification, we divided~~

229 ~~nitrate into two separate pools, denoted s-NO$_3$$^=$ for nitrate transported from the surface water~~

230 ~~and g-NO$_3$$^=$ for nitrate from upwelling groundwater.~~ The biogeochemical reactions<u>:</u> ~~are~~

231 aerobic respiration (AR), non-mixing-dependent, and mixing-dependent denitrification (DN) <u>are</u>

considered in the reactive transport model:

$$AR: CH_2O + O_2 \rightarrow CO_2 + H_2O \tag{R1}$$

$$DN: CH_2O + 0.8NO_3^- + 0.8H^+ \rightarrow CO_2 + 1.4H_2O + 0.4N_2 \tag{R2}$$

Equations R1 and R2, with DOC as the electron donor and O_2 and NO_3^- as sequential electron acceptors, capture the primary mechanism of NO_3^- cycling and are widely used in studies on hyporheic zone nitrogen dynamics (Bardini et al., 2012; Hester et al., 2019; Zheng et al., 2019). Denitrification is the well-recognized critical process for NO_3^- transformation and reduction in riparian and hyporheic zones. The reaction stoichiometry and electron acceptor utilization order in R1 and R2 match well-established principles from lab incubations and field investigations (Hedin et al., 1998; Liu et al., 2017; Zarnetske et al., 2011a, 2011b). Dissimilatory nitrate reduction to ammonium (DNRA) and anaerobic ammonium oxidation (ANAMMOX) are not included in the model, as these processes play secondary role on nitrogen cycling and require highly specific conditions to occur (Zarnetske et al., 2012). Ammonia (NH_4^+) was excluded, as it is unstable in the study environment: NH_4^+ in surface water or groundwater is prone to nitrification (converting NH_4^+ to NO_3^-) either within hyporheic flow cells or in upwelling groundwater upon O_2 exposure, leading to relatively low NH_4^+ concentrations (Hester et al., 2014).

Reaction rates were defined using Monod kinetics (Monod, 1949Zarnetske et al., 2012):

$$R_{AR} = V_{AR} \times X_{AR} \times \frac{c_{O_2}}{c_{O_2} + K_{O_2}} \times \frac{c_{DOC}}{c_{DOC} + K_{DOC}} \tag{64}$$

$$R_{DN} = V_{DN} \times X_{DN} \times \frac{c_{NO_3^-}}{c_{NO_3^-} + K_{NO_3^-}} \times \frac{c_{DOC}}{c_{DOC} + K_{DOC}} \frac{K_{inh}}{K_{inh} + c_{O_2}} \tag{57}$$

252   The reaction terms R_i was given by

$$R_{s-NO_3^-} = -R_{DN}(c_{s-NO_3^-})$$ (8̶6̶)

253

$$R_{g-NO_3^-} = -R_{DN}(c_{g-NO_3^-})$$ (9̶7̶)

254

$$R_{O_2} = -R_{AR}$$ (1̶0̶8̶)

255

$$R_{DOC} = -R_{AR} - 0.8 \times (R_{DN}(c_{s-NO_3^-}) + R_{DN}(c_{g-NO_3^-}))$$ (1̶1̶9̶)

256

257   where V_{AR} and V_{DN} [T^{-1}] are the maximum reaction rate of AR aerobic respiration and DN–

258   denitrification, X_{AR} and X_{DN} [M L^{-3}] are the biomass of functional microbial groups facilitating

259   the reaction components of AR and DN. K_{inh} [M L^{-3}] is a non-competitive inhibition factor used

260   for representing inhibition of DN given oxygen availability.

261   2.2.2   Boundary condition

262   The hydraulic head imposed along the top boundary was described as a sinusoidal function

263   that moves downstream by the ripple migration velocity (u_c [L T^{-1}]; Boano et al., 2013):

$$h\big|_{y=l} = h_m \cdot \sin m(x - u_c dt)$$ (10)

264

265   where m [-] is the wave number of the variation ($m = 2\pi/\lambda$), dt [T] denotes a timestep in the

266   simulation, and h_m [L] is the amplitude of the head variation (Elliott and Brooks, 1997):

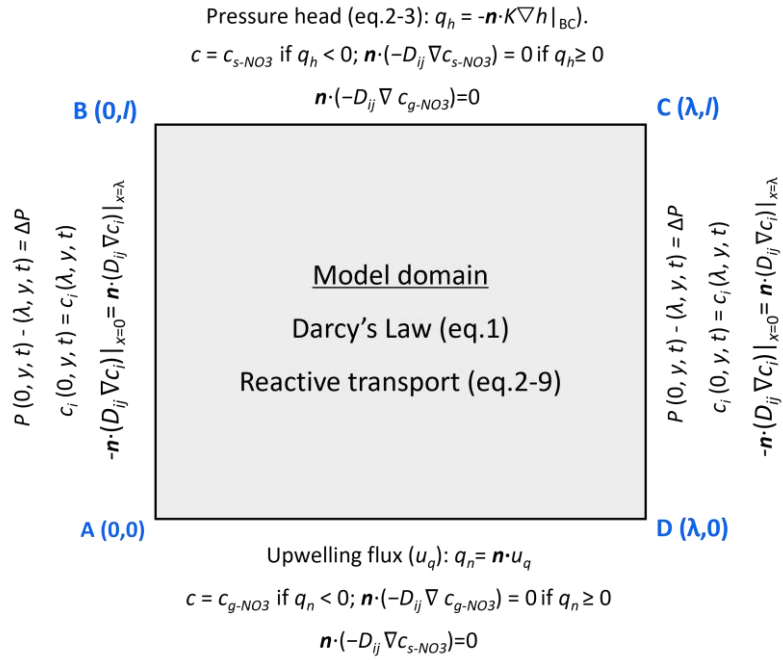$$h_m = a \frac{U^2}{2g}\left(\frac{H_d/H}{0.34}\right)^e$$ (11)

267

268   where $a = 0.28$ [-] is a dimensionless coefficient, U [L T^{-1}] is the average stream velocity, H_d [L]

269   is the height of the ripple, H [L] is the water depth. The exponent e equals to 3/8 if $H_d < 0.34H$

270   and 3/2 otherwise.

19

Given the periodic characteristics typically observed in riverbeds under field conditions (Ahmerkamp et al., 2017; Harvey et al., 2012), a single ripple was chosen in this study. Periodic pressure and solute boundary conditions were applied to side boundaries AB and CD to replicate the repetitive geometric constraints of the streambed. This is a well-established practice in hyporheic exchange modeling, as it minimizes edge effects without the need for computationally intensive full-scale simulations of multiple consecutive bedforms:~~The lateral boundaries AB and DC were set to be periodic boundaries:~~

$$P(0, y, t) = P(\lambda, y, t) + \Delta P \qquad (12)$$

$$c_i(0, y, t) = c_i(\lambda, y, t) \quad \boldsymbol{n} \cdot \left(-D_{ij} \nabla c_i\right)\big|_{x=0} = \boldsymbol{n} \cdot \left(D_{ij} \nabla c_i\right)\big|_{x=\lambda} \qquad (13)$$

where P [M L^{-1}T^{-2}] is the pressure calculated using the hydrostatic head from equation (10), $P = \rho g h$. ~~$P(0, y, t) = P(\lambda, y, t) + \Delta P$, $c_i(0, y, t) = c_i(\lambda, y, t)$ and $\partial c_i(0, y, t)/\partial y = \partial c_i(\lambda, y, t)/\partial y$.~~ The additional pressure drop ΔP [M L^{-1}T^{-2}] was~~is~~ derived from the streambed gradient and calculated using $\Delta P = S \rho g \lambda$. For the validation of model generalization, simulation of three consecutive ripples was conducted. The middle ripple was focused on to compare its vertical boundary-related pressure and solute concentration with outcomes from the single-ripple model. Simultaneously, comparisons were made between the two models (single-ripple and three-consecutive-ripple) regarding simulated riverbed flow fields, nitrate plumes, influxes, and reaction rates. Although moderate left/right boundary pressure differences were detected between their simulation results, such variations had negligible effects on reactive solute transport. This comparison is provided in the Supporting Information (Text S2).

At the top boundary:

Pressure head (eq.2-3): $q_h = -\boldsymbol{n} \cdot K \nabla h |_{BC}$.

$c = c_{s\text{-}NO3}$ if $q_h < 0$; $\boldsymbol{n} \cdot (-D_{ij} \nabla c_{s\text{-}NO3}) = 0$ if $q_h \geq 0$

$\boldsymbol{n} \cdot (-D_{ij} \nabla c_{g\text{-}NO3}) = 0$

B (0,l) — C (λ,l)

Left boundary:

$P(0, y, t) - (\lambda, y, t) = \Delta P$

$c_i(0, y, t) = c_i(\lambda, y, t)$

$-\boldsymbol{n} \cdot (D_{ij} \nabla c_i)|_{x=0} = \boldsymbol{n} \cdot (D_{ij} \nabla c_i)|_{x=\lambda}$

Model domain

Darcy's Law (eq.1)

Reactive transport (eq.2-9)

Right boundary:

$P(0, y, t) - (\lambda, y, t) = \Delta P$

$c_i(0, y, t) = c_i(\lambda, y, t)$

$-\boldsymbol{n} \cdot (D_{ij} \nabla c_i)|_{x=0} = \boldsymbol{n} \cdot (D_{ij} \nabla c_i)|_{x=\lambda}$

A (0,0) — D (λ,0)

Upwelling flux (u_q): $q_n = \boldsymbol{n} \cdot u_q$

$c = c_{g\text{-}NO3}$ if $q_n < 0$; $\boldsymbol{n} \cdot (-D_{ij} \nabla c_{g\text{-}NO3}) = 0$ if $q_n \geq 0$

$\boldsymbol{n} \cdot (-D_{ij} \nabla c_{s\text{-}NO3}) = 0$

Figure 2. Schematic diagram of the simulated domain and boundary conditions.

At the bottom boundary, an upward groundwater flux was defined to mimic the process of groundwater discharge. For groundwater borne nitrate, the bottom boundary ~~The top boundary BC was~~ was specified as an open Dirichlet boundary with constant g-NO$_3^-$ ~~solute~~ concentrations in groundwater: ~~the stream.~~

$$\begin{cases} c = c_i & \boldsymbol{n} \cdot \boldsymbol{v} < 0 \\ \boldsymbol{n} \cdot \left(-D_{ij} \nabla c_i \right) = 0 & \boldsymbol{n} \cdot \boldsymbol{v} \geq 0 \end{cases} \tag{14}$$

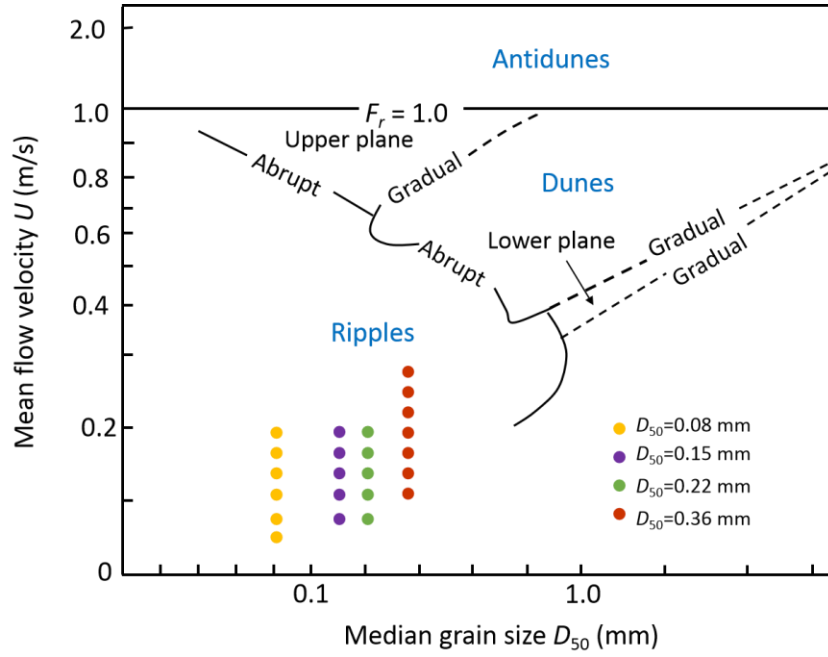where the outward unit normal is n. Besides, the top boundary for the g-NO$_3^-$ was assigned as outflow condition.

For stream-borne solutes includes DOC, O$_2$, and s-NO$_3^-$, an open boundary with a constant solute concentration was imposed on the top boundary, and outflow boundary was applied on the bottom of the domain. The concentrations of the all solutes were initially assumed to be zero. A quantitative mass-balance check for the model was included in Supporting Information

21

Text S2.

~~An upward groundwater flux with constant nitrate concentration was specified at the bottom boundary AD to mimic a nitrate polluted groundwater discharge.~~

2.3 Bedform migration

In this study, ripples formation was qualitatively determined using the bedform stability diagram (Figure 3). This diagram is a summarized reference for examining equilibrium bed configurations in unidirectional flow, derived from a series of flume experiments and field studies (Ashley, 1990). Besides, a series of quantitative criteria (Text S1 in the supporting information: Criteria for ripple migration) was examined to ensure ripple formation under the modeled scenarios and the achievement of dynamic equilibrium~~The mechanisms of bedform initialization, formation and migration are initiated through a set of criteria to ensure that ripples are expected to form under the modeled scenarios and reach a state of dynamic equilibrium, where the ripples remain mobile while maintaining their shape. The development of ripples is assessed under different conditions of median particle size D_{50} and flow velocity based on a set of quantitative criteria (as reference in Ping et al., 2022 for criteria on ripple formation)~~. For a specific grain size of streambed sediment (D_{50}), particular stream velocities (U) satisfying ~~that fulfill~~ all these criteria ~~for the development of ripple bedforms that are mobile under dynamic equilibrium~~ are selected and displayed in ~~(~~Figure ~~–~~ 3~~2)~~. All simulation scenarios were listed in the Table S1~~3. in the supplementary material.~~

323

Figure 32. The bedform stability diagram (modified from Ashley, 1990) showing the bedform

properties and hydraulic conditions considered in this study.

Ripple migration velocities ~~are~~ were implemented using an empirical relation after Coleman

and Melville (1994), which was derived from flume experiments:

$$\frac{u_c}{\left(u^* - u_{cr}^*\right)\left(\tau^* - \tau_{cr}^*\right)}\left(H_d / D_{50} - 3.5\right)^{1.3} = 40$$

(15)

where ~~D_{50} [L] is the median grain size,~~ $u^* = (gHS)^{0.5}$ [L T^{-1}] is the bed shear velocity, S [-] is the

stream gradient and calculated by Chezy equation ($U = H^{2/3}S^{1/2}/n$, where n [-] is the Manning

coefficient and assumed to be 0.02 for sand). u_{cr}^* [L T^{-1}] is the critical bed shear velocity and it

can be calculated by the critical Shield parameter τ_{cr}^* ($\tau_{cr}^* = \tau_{cr} / g(\rho_s - \rho)D_{50}$, $u_{cr}^* = (\tau_{cr} / \rho)^{0.5}$, ρ_s

[M L^{-3}] and ρ [M L^{-3}] are the density of sediment and water), and τ^* is the shield number related

to the bed shear velocity ($\tau^* = u^{*2}/rgD_{50}$; r [-] is the submerged specific gravity of sediment = (ρ_s

$- \rho)/ \rho$). The critical shields parameter τ_{cr}^* defines the threshold for the initialization of motion,

and it is determined by the dimensionless particle parameter D^* [-] (Soulsby, 1997; Zheng et al.,

23

2019):

$$\tau_{cr}^{*} = \frac{0.3}{1+1.2D^{*}} + 0.055\left[1 - \exp\left(-0.02D^{*}\right)\right]$$

(16)

where $D^{*} = D_{50} \cdot (rg/v^2)^{1/3}$, v is the kinematic viscosity of water [L^2 T^{-1}]; The derived celerity was

substituted into Equation (10) to determine the migration of sinusoidal head profile with ripples

moving.

2.4 Governing non-dimensional numbers

The characteristics of the modeled system were depicted by a series of non-dimensional

numbers, which represent the relative dominance of various forces, transport, and reaction

processes in this system. Firstly, ~~we used~~ the Reynolds number Re was used to characterize the

flow condition of surface water (Cardenas and Wilson, 2006):

$$Re = \frac{UH_d}{v}$$

(17~~3~~)

where v [L^2 T^{-1}] represents kinematic viscosity of water.

~~TWe introduced t~~he dimensionless parameter U_r [-] was introduced to represent the relative

magnitude of bedform celerity and the pressure-induced pore water velocity driven by pressure

variation over the ripple surface and upwelling groundwater:

$$U_r = \frac{\theta \cdot u_c - u_s}{u_p}$$

(18~~4~~)

where u_s [L T^{-1}] is the seepage velocity of the underflow induced by stream gradient ($u_s = KS$),

and thus the characteristic horizontal velocity is $u_c - u_s/\theta$. u_p/θ [L T^{-1}] is the pore water velocity

induced by pumping process and is calculated using the analytical solution after Boano et al.

356 (2009) and Fox et al. (2014) accounting for vertical groundwater flux (u_q [L T^{-1}]):

$$u_p = u_{p,0}\sqrt{1-\left(u_q/\pi u_{p,0}\right)^2} + \left(\left|u_q\right|/\pi\right)\sin^{-1}\left(\left|u_q\right|/\pi u_{p,0}\right) - \left(\left|u_q\right|/2\right)$$

357 (19 ~~5~~)

$$u_{p,0} = a\frac{KU^2}{g\lambda}\left(\frac{H_d/H}{0.34}\right)^m$$

358 (20 ~~16~~)

359 where $u_{p,0}$ [L T^{-1}] represents the hyporheic exchange solely driven by pressure variation over the

360 sediment-water interface; if $U_r > 1$, turnover process dominates and controls the hyporheic

361 exchange, otherwise, the system is pumping process dominated (Jiang et al., 2022).

362   The relative magnitude of hyporheic exchange flux driven by pressure variation along the

363 riverbed~~ripple~~ surface and upwelling groundwater flux was~~is~~ determined as:

$$U_b = \frac{u_q}{u_{p,0}}$$

364 (21 ~~17~~)

365   The relative dominance of hyporheic exchange and biogeochemical reaction in nitrate

366 removal can be defined by the Damköhler number (Ocampo et al., 2006; Zarnetske et al., 2012;

367 Zheng et al., 2019):

$$Da = \frac{\tau_T}{\tau_R}$$

368 (22 ~~18~~)

369 the characteristic timescale for the transport of solutes through the ripple was~~is~~ estimated as

370 (Azizian et al., 2015):

$$\tau_T = \frac{\lambda\theta}{\pi^2 u_p}$$

371 (23 ~~19~~)

372 and the reaction timescale (τ_R) represents the time needed to consume dissolved oxygen of

373 hyporheic water to a prescribed anoxic environment threshold (2 mg/L). The reaction timescale

25

374　was~~is~~ described as:

$$\tau_R = \frac{\ln\left(c_{O_2}/c_{O_2,\text{lim}}\right)}{V_{AR}}$$　　　　　(2**4**0)

376　biogeochemical reactions are transport-limited when $Da < 1$. The biogeochemical reactions

377　depended on reaction kinetics due to the brevity of the time that reactants spend within the HZ.

378　Under these low Da conditions, the HZ remains oxic conditions, resulting in a minimal or no

379　denitrification to occur. Conversely, when $Da > 1$, the residence time of reactants exceeds the

380　reaction time, and thus oxygen is consumed and favors for the occurrence of denitrification in

381　anoxic conditions (Jiang et al., 2022; Zarnetske et al., 2011a).

382　**2.5 Model setup and parametrization**

383　　　All parameter values in this study were shown in Table 1. The bedform geometry of Ping et

384　al. (2022) was adopted for this study (~~streambed length and height: $\lambda = 0.2$ m and $l = 0.16$ m;~~ the

385　ripples located at $\lambda_c = 0.15$ m with a height of $H_d = 0.02$ m). Here grain sizes D_{50} of 0.08, 0.15,

386　0.22 and 0.36 mm were considered, typically falling within characteristic grain diameters on

387　sandy riverbeds (Ahmerkamp et al., 2017; Harvey et al., 2012). The permeability of riverbed

388　was calculated using ~~We used~~ the empirical relation $k = Da'\times735\times10^6\times D_{50}^2$ (where $Da' =$

389　9.869×10^{-13} is the conversion factor for unit Darcy to m^2; Gangi, 1985).

390　　　The concentrations of DOC, O_2, and s-NO_3^- in stream were specified as 30 mg/L, 8 mg/L,

391　and 5 mg/L. This configuration represents a pristine stream characterized by moderate nutrient

392　levels (Ocampo et al., 2006). The g-NO_3^- in groundwater was set as 15 mg/L, representing the

393　chemical signature of nitrate-contaminated groundwater that lacks both oxygen and organic

matter (Hester et al., 2014). The maximum reaction rate and corresponding functional microbial

concentration for AR and DN ~~were~~are listed in Table 1, the choose biogeochemical values are

consistent with the parameter setting of nutrient cycling in hyporheic zones and riparian zones

(Gu et al., 2008; Nogueira et al., 2021; Zarnetske et al., 2012).

Table 1. Model parameters used in numerical simulations

Parameter	Description	Value
l [m]	Streambed depth	0.16 [a, b]
l_c [m]	Ripple crest	0.15 [a, b]
λ [m]	Wavelength of ripple	0.2 [a, b]
H_d [m]	Height of ripple	0.02 [a, b]
H [m]	Stream water depth	0.1 [a, b]
θ [1]	Porosity	0.38 [e]
α_L [m]	Longitudinal dispersivity	0.01 [f]
α_T [m]	Transverse dispersivity	0.001 [f]
K_{inh} [mg L^{-1}]	Inhibition constant	0.25 [c, d]
K_{DOC} [mg L^{-1}]	Half-saturation constant for dissolved organic carbon	6 [c, d]
K_{NO3} [mg L^{-1}]	Half-saturation constant for nitrate	1 [c, d]
K_{O2} [mg L^{-1}]	Half-saturation constant for dissolved oxygen	0.5
V_{DN} [h^{-1}]	Maximum specific uptake rate for denitrification	1 [c, d]
V_{AR} [h^{-1}]	Maximum specific uptake rate for aerobic respiration	2 [c, d]
C_{DOC} [mg L^{-1}]	Concentration of dissolved organic carbon in stream	30
C_{O2} [mg L^{-1}]	Concentration of dissolved oxygen in stream	8

$C_{\text{s-NO3}^-}$ [mg L^{-1}]	Concentration of nitrate in stream	5
$C_{\text{g-NO3}^-}$ [mg L^{-1}]	Concentration of nitrate in groundwater	15

[a] Janssen et al. (2012) [b] Ping et al. (2022) [c] Zarnetske et al. (2012) [d] Sawyer (2015) [e] Ahmerkamp et al. (2015) [f] Bardini et al. (2012)

The following distinct model experiments were carried out: The Reynolds number, i.e., mean stream velocity, was varied for Re = 2000–6000 in intervals of 500, with corresponding stream water velocities of U = 0.1–0.3 m/s. The range of U_b was set from 0.3 to 0.7 in intervals of 0.1; 1. correspondingly, the upwelling groundwater flux u_g was ranged between 0.3×$u_{p,0}$ and 0.7×$u_{p,0}$. A larger upward flux than 0.9×$u_{p,0}$ would eliminate the entire hyporheic flow cell, thus we set the maximum boundary flux was set at a value slightly below this threshold. Meanwhile a minimum of 0.2×$u_{p,0}$ ensures that upwelling groundwater is still mixing with surface water with minor influences on hyporheic flow cell.

The finite element software, COMSOL Multiphysics (version 6.1) was used to solve the Darcy flow and multi-component solute transport model. Three computational grids were evaluated to ensure grid resolution independence of simulated results, confirming that the grid is sufficiently refined to capture mixing dynamics and minimize numerical dispersion. The fine, base and coarse grid sizes were 1.5 mm, 2 mm, and 2.5 mm, respectively. The grid independence analysis was provided in the Supporting Information (Text S2). For the simulations, the base grid size was selected, with the domain discretized into 19,940 cells. The domain was discretized with a grid spacing from 4×10^{-4} to 0.2 cm, the resultant mesh consisting of 19,940 elements. To maintain a constant bedform displacement (Δx) per timestep, the simulation was conducted with Δx = 2 mm, while dt was adjusted in inverse proportion to the

419   migration celerity u_c. The total duration of the simulation was set to be equal to the time needed

420   for hundreds of ripples to travel across the modeled domain until the hyporheic exchange and

421   biogeochemical processes reached quasi-steady states.

2.6 Model Metrics

2.6.1 Mixing of surface water and groundwater

424   Here, macroscopic mixing is defined as the colocation of surface water (SW) and

425 groundwater (GW) within a specific aquifer volume (e.g., a numerical model element or cell), a

426 process that causes solutes to be present simultaneously in an overlapping region (Nogueira et

427 al., 2022). There is no established standard for the threshold governing SW and GW fractions

428 during the mixing process; nonetheless, the general recognition is that mixing occurs when the

429 GW proportion falls within the range of 10% to 90% (Hester et al., 2013; Woessner et al., 2000).

430 This interval effectively distinguishes the occurrence of mixing, where SW and GW interact

431 dynamically, from the two endmembers: pure GW (>90%) and pure SW (<10%). To evaluate

432 the influence of threshold variations on mixing metrics, sensitivity analysis was conducted to

433 examine three alternative GW fraction ranges: 10%–90% (wider interval), 16%–84%, and 20%–

434 80% (narrower range). Thus, mixing flux and mixing zone were calculated based on these three

435 thresholds.

436 ~~Mixing occurs at the interface between regions of advected surface water and upwelling~~

437 ~~groundwater, where the flow paths from these two sources run parallel to each other.~~ A ~~We~~

438 ~~specified a~~ constant concentration of conservative tracer (c_{gw} = 1 mg/L) in ~~groundwater~~GW was

439 specified to represent the tracer signature of groundwater, following the methods outlined by

Hester et al. (2013, 2014). ~~The tracer plume is used to visualize the surface water and groundwater mixing size and calculate the mixing magnitude quantitatively. The mixing zone is defined as the area where the groundwater proportion varies between 16% and 84% (Santizo et al., 2020). The size of the surface water and groundwater mixing zone (A_{mix}) was calculated by integrating the area where the concentration of the conservative tracer ranges from 0.16 to 0.84 mg/L.~~

The groundwater-borne tracer~~amount of tracer mass~~ that undergoes mixing as it transitions from flow paths originating at the bottom boundary to those emerging at the streambed surface was quantified to determine the net effect of mixing ~~occurring along the entire length of the mixing zone~~. The streambed surface was divided into three zones (Figure 1): "SW IN", where surface water enters the riverbed layer~~bed~~; "SW OUT", where surface water discharges back into the overlying water column; and "GW OUT", where upwelling groundwater discharges into the stream. The conservation tracer ~~mass~~ flux for the SW OUT zone was used to describe mixing. If no mixing occurred, all the conservative tracer ~~mass~~ entering the model at the bottom boundary would exit through the GW OUT zone on the riverbed~~streambed~~ surface~~e~~. ~~The mixing flux (MF) across the sediment-water interface was determined by integrating the Darcy flux flowing outward through the SW OUT zone, representing the total cumulative effect of mixing along the entire length of the mixing zone (Hester et al., 2013).~~ The arrival of conservative solute at the riverbed surface is defined as the start of mixing, and the complete leave of all the conservation solute from the riverbed is defined as the end of mixing. The mixing flux across the riverbed surface was determined by integrating the outward volumetric flux containing groundwater-borne conservation solute within the specified concentration range (i.e., $c_{gw} = 0.1$

0.9 mg/L, c_{gw} = 0.16–0.84 mg/L, c_{gw} = 0.2–0.8 mg/L). This flux corresponds to groundwater

flowing through "SW OUT" zone. Concurrently, the mixing zone was calculated by integrating

the riverbed area that contains groundwater-borne conservation solute within the specified

concentration range. The average flux and zone over this mixing period were computed and

termed the mixing flux (*MF*) and mixing zone, respectively.

The mixing fraction (*Fmix*) was computed as the ratio of the mixing flux to the total

hyporheic flux, which was derived from integrating the volumetric flux along the sediment-

water interface (including both SW OUT and GW OUT). ~~This total flux is triggered by both~~

~~pumping and bedform migration, and is simultaneously influenced by upwelling~~

~~groundwater~~*Fmix* serves as a metric to quantify the proportion accounted for by the SW-GW

mixing flux within the overall flux of SW and GW interaction across the sediment-water

interface. *Amix* is defined as the ratio of the mixing zone to the entire modeled domain,

representing the proportion of the riverbed occupied by the mixing zone.

~~The mixing zone is defined as the area where the groundwater proportion varies between~~

~~16% and 84% (Santizo et al., 2020). The size of the surface water and groundwater mixing zone~~

~~(A_{mix}) was calculated by integrating the area where the concentration of the conservative tracer~~

~~ranges from 0.16 to 0.84 mg/L.~~

2.6.2 Nitrate reaction rate and efficiency

When the hydro-physical and biogeochemical conditions reach a quasi-steady state, ~~we~~

~~select the last 10 periods of ripple migration and calculate~~ the average flux of ~~total amount of~~

stream- or groundwater- borne nitrate entering ~~being induced into~~ the riverbed layer over the

31

483   final ~~during~~ serval periods of ripple migration~~the time interval~~ was calculated:

$$M_{in,s-NO_3^-} = \frac{1}{w}\sum_T B\int vc_{s-NO_3^-} - \theta D_{ij} \cdot \nabla c_{s-NO_3^-} dL_{top} \tag{25$\underline{1}$}$$

$$M_{in,g-NO_3^-} = \frac{1}{w}\sum_T B\int vc_{g-NO_3^-} - \theta D_{ij} \cdot \nabla c_{g-NO_3^-} dL_{bottom} \tag{26$\underline{2}$}$$

486   where B [L] is the per unit width, $\underline{\theta}$ [-] is the sediment porosity, and $w = T/dt$ [-]$\underline{;}$ ~~, F_{SWI} [L T^{-1}] is~~

487 ~~the inward flux across the ripple surface~~$\underline{L_{top}}$ and $\underline{L_{bottom}}$ refer to the top boundary BC and bottom

488 boundary AD, respectively.~~.~~

489   The total amount of nitrate removed by ~~non-mixing-dependent (~~NMD~~)~~ denitrification and

490 ~~mixing-dependent (~~MD~~)~~ denitrification $\underline{were}$ ~~are~~ calculated as follows during the same time

491 interval:

$$M_{NMD} = \frac{1}{w}\sum_T B\int R_{DN}(c_{s-NO_3^-})dA \tag{27$\underline{3}$}$$

$$M_{MD} = \frac{1}{w}\sum_T B\int R_{DN}(c_{g-NO_3^-})dA \tag{28$\underline{4}$}$$

494   where A [L^2] is the area of the streambed.

495     $\underline{\text{Nitrate removal efficiency was quantified as the rate of nitrate removed from the riverbed}}$

496 $\underline{\text{layer divided by the nitrate flux entering the riverbed layer}}$~~The nitrate removal efficiency is~~

497 ~~defined as the ratio of the amount of nitrate being removed by DN to the amount of nitrate being~~

498 ~~induced into the riverbed~~:

$$N_{RE-NMD} = \frac{M_{NMD}}{M_{in,s-NO_3^-}}, \quad N_{RE-MD} = \frac{M_{MD}}{M_{in,g-NO_3^-}}$$

499 $$\tag{29$\underline{5}$}$$

3. Results

3.1 Model validation

3.1.1 Validation of flat bed model with triangular ripple model

Model validation was conducted in two steps, with two numerical methods employed to represent moving bedforms. Beyond simulating porewater flow and reactive solute transport in a fixed frame of reference with a flat riverbed surface, a reference frame moving with triangular ripples was also adopted to capture bedform migration, following the methods of Bottacin-Busolin and Marion (2010), Ahmerkamp et al. (2015), and Kessler et al. (2015). The latter method captures bedform migration while preserving the ripple shape, and comparisons between the two approaches were conducted to examine the impact of neglecting ripple geometry on the simulated results.

A typical case ($Re = 3000$, $U_b = 0.6$ and $D_{50} = 0.15$ mm) was chosen here for comparison. The overall patterns of pressure head, Darcy velocity, and stream-borne solute plume distributions were mostly similar (Figure 4). The difference in groundwater-borne nitrate plumes is attributed to the distinct advection velocities for reactive solute transport. Specifically, the moving reference frame involves a transformation of the horizontal coordinate system, based on the assumption that the frame of reference moves in the direction of bedform migration and at the same migration celerity; in this frame, the modeled advection velocity of reactive solutes is the seepage velocity minus the celerity. Thus, in the triangular ripple model, g-NO_3^- flows upstream with larger advection velocities, resulting in a more uniform solute plume; in contrast, it exits the riverbed across the entire riverbed surface in the flat bed model (see the white

streamlines). Correspondingly, discrepancies emerge in the crest area of the MD denitrification

522   zone.
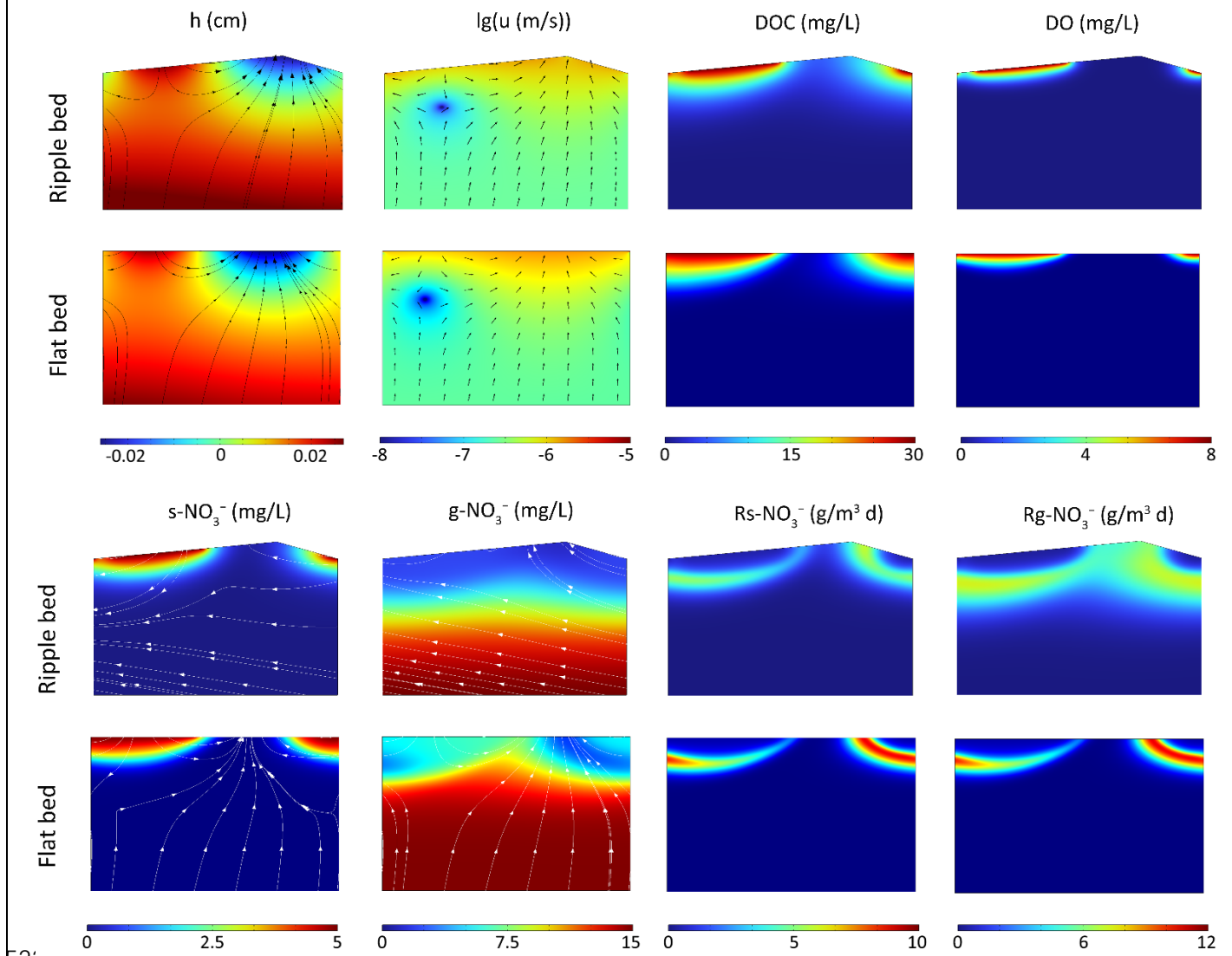
Figure 4. Comparison of hyporheic flow and reactive solute transport modeling results from the

flat bed model and the triangular ripple model. Streamlines and arrows in the Darcy flow field

indicate porewater flow, while streamlines in nitrate solute plumes represent the advection

velocity of reactive solute transport.

Compared with the triangular ripple model, the flat bed model exhibit slightly larger

hyporheic exchange flux, mixing flux, and stream-borne nitrate influx. The relative errors are

approximately 10%. Meanwhile, both the MD and NMD denitrification rates are higher in the triangular ripple model than in the flat bed model, with relative errors around 20%. Differences in the results of the simulated domain cause subtle changes in flow and transport processes, changes that are acceptable for our intended purposes. To further assess the differences between the two models and their reliability, two methods were utilized to perform validation against the experiments by Wolke et al. (2020).

3.1.2 Validation of numerical models with laboratory experiments

The developed models ~~model development~~ wereas validated through ~~by~~ comparison with ~~to~~ ~~flume experiments of~~ Wolke et al.'s (202019) flume experiments, which investigated the evolution of oxygen in the riverbed under varying conditions ~~that were conducted to study the~~ ~~evolution of oxygen in the riverbed under different conditions~~ of mean stream velocity (0.16−0.32 m/s) and bedform migration celerity (0−0.394 cm/h). ~~No upwelling flux of~~ ~~groundwater was considered at the bottom of the riverbed.~~ The experiment was designed with a total of 5 operating conditions, each of which was repeated twice and labeled as Set 1 and Set 2. Oxygen distribution within sediments was measured via planar optodes, and the oxygenated zone was defined as regions where oxygen saturation exceeds 15%. Oxygen consumption was observed within riverbed layer and aerobic respiration is widely recognized as the dominant process driving oxygen consumption within riverbed sediments (Ahmerkamp et al., 2017; Reeder et al., 2018). In their experiments, a fixed amount of NaCl was added to surface water; this NaCl was then used to compute hyporheic exchange flux (HEF) from the decline in its concentration, following the method by Fox et al. (2018). The oxygen influx (F_{in}) and outflux

552 (F_{out}) were calculated by multiplying *HEF* by the surface water oxygen concentration and the

553 mean oxygen concentration in the oxygenated zone, respectively.

554 ~~Based on the criteria for ripple migration, it was determined that under the hydraulic~~

555 ~~conditions of Run 5, ripples could not migrate while maintaining their shapes due to increased~~

556 ~~flow intensity. Therefore, the model validation simulations considered four hydraulic conditions~~

557 ~~of Run 1 to 4.~~

(a) U = 0.16 cm/s   (b) U = 0.25 cm/s   (c) U = 0.28 cm/s   (d) U = 0.32 cm/s

Ripple model

Flat model

O_2 (mol/m³)

(e) HEF (cm/d) — Experiment, Ripple model, Flat model — RMSE = 2.83

(f) Ao (cm²) — Experiment, Ripple model, Flat model — RMSE = 4.76

(g) F_{in} (mmol/m²d) — Experiment, Ripple model, Flat model — RMSE = 5.75

(h) F_{out} (mmol/m²d) — Experiment, Ripple model, Flat model — RMSE = 7.36

37
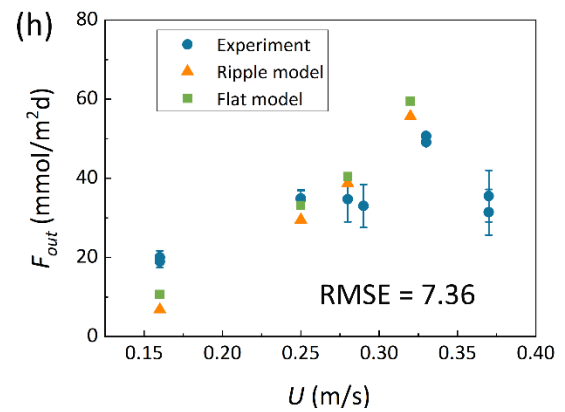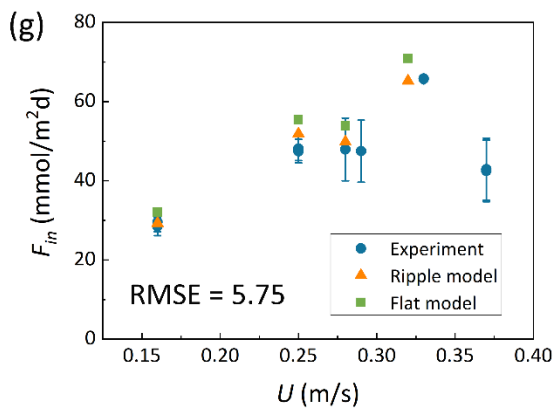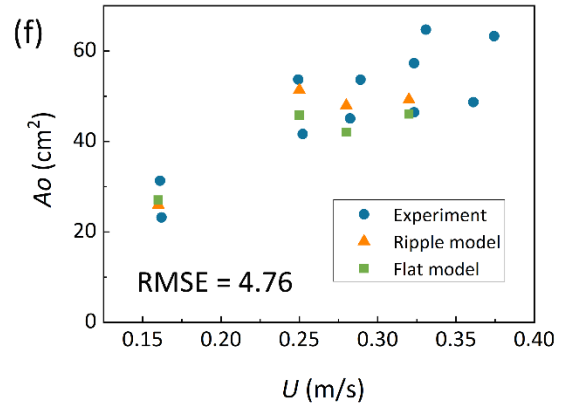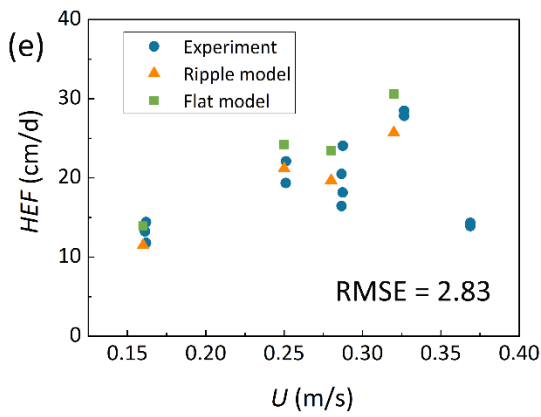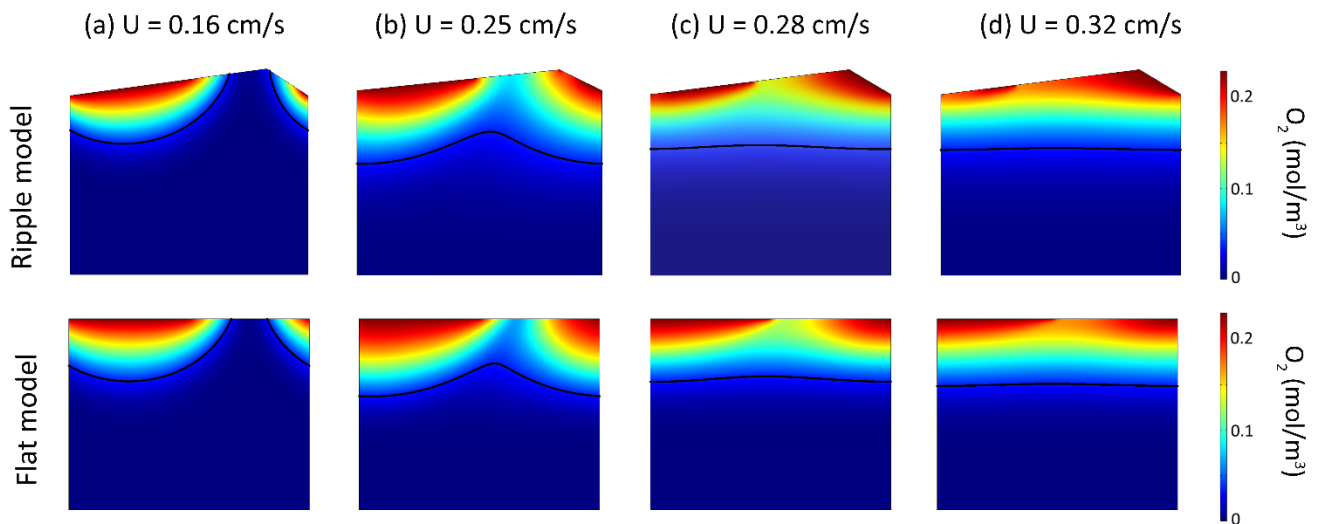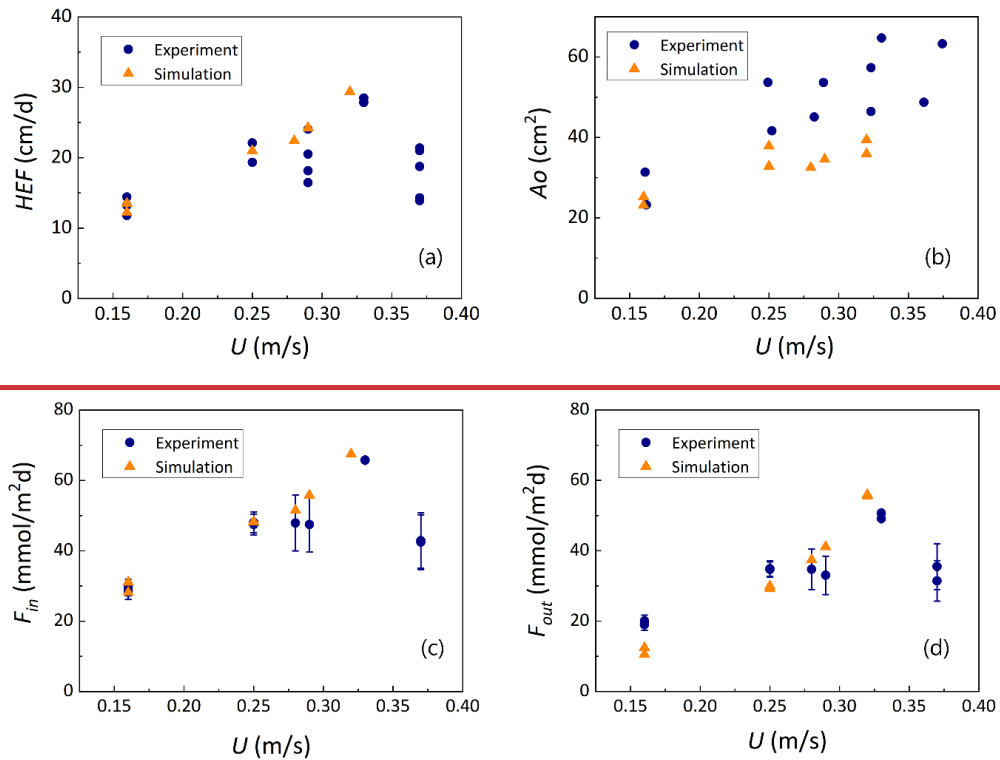
Figure 53. Comparison of numerical modeled (a) hyporheic exchange flux, (b) summed oxic zone and (c) oxygen influx and (d) oxygen outflux and experimental measurements by Wolke et al. (2020) under various conditions.

Two numerical models: the flat bed model and the triangular ripple model, were developed under the same hydraulic conditions, with their parameters adjusted to fit HEF, F_{in}, F_{out}, and A_O to experimental data. In the numerical model, HEF was calculated by integrating the volumetric flux over the inflow zones along the sediment-water interface. Oxygen transport was governed by the advection-dispersion-reaction equation, where oxygen consumption occurred through aerobic respiration following the Monod kinetics described by Equation (8). The F_{in} and F_{out} were then computed by multiplying the HEF by the oxygen concentration in the surface water and the oxygen concentration over the outflow zones along the riverbed surface, respectively. The oxygenated area was calculated by integrating the riverbed portions where oxygen saturation exceeds 15%. Based on the criteria for ripple migration, it was determined that under

the hydraulic conditions of Run 5, ripples could not migrate while maintaining their shapes due to increased stream flow velocity. Therefore, the model validation simulations considered four hydraulic conditions of Run 1 to 4. The model parameters used and adjusted were summarized in Supporting Information Text S3: Model Calibration.

~~The parameters used for model validation are shown in supporting information Table S1 and S2.~~ For stationary and slow-migrating beds, the spatial distribution of oxygen creates a conchoidally shaped plume beneath the bedform; in contrast, beneath fast-migrating beds, the oxygen plume shifts to a more uniform front. The HEF, F_{in}, F_{out}, and A_O simulated using both the ripple bedform model and the flat bed model were presented in Figure 5; these results are in good qualitative and quantitive agreement with the measurements of Wolke et al. (2020). The root means square error (RMSE) were further calculated between the experimentally measured values and those simulated by the flat bed model. All RMSE values fall within reasonable ranges, indicating the critical processes of bedform migration and oxygen dynamic are captured by the numerical models. ~~In stationary and slow-migrated beds, the spatial distribution of oxygen creates a typical conchoidally-shaped plume in the riverbed. In contrast, for fast-migrated beds, the oxygen plume becomes a more uniform front (Ping et al., 2022). The comparison of modeled oxygen distributions with experimental measurements reveals that simulated values of the oxygenated zone was slightly lower than observed. This discrepancy is mainly attributed to two factors: firstly, the dissolved oxygen concentrations measured by the planar optode system were relatively high, as noted in Wolke et al. (2019) themselves. Secondly, only oxygen fluxes within immobile riverbeds were simulated and did not include the areas of the mobile sections in the numerical modeling. Because the mobile riverbeds exist in oxygen-~~

3.2 Effect of bedform migration on mixing regimes and solute dynamictransport

To simulate the range of natural environmental conditions, the reactive transport equations

were solved for different stream velocities, grain sizes and groundwater upwelling fluxes, which

include a corresponding range of ripple migration celerites and sediment permeabilities derived

from the empirical relations. As an example, the patterns of pore water transport as well as SW

and GW mixing are shown for a grain size of 0.15 mm, a constant ratio between pumping driven

hyporheic exchange flux and upwelling GW flux $U_b = 0.6$ and four different stream velocities,

that is four different Re numbers.

For low surface water flow velocity ($Re = 2500$, $U = 0.125$ m/s), no migration of bedform

iwas predicted by the model. SW enters the riverbed layer sediment in the high-pressure region

on the stoss side, flows through the porous medium, and exits the riverbed layerbedform in the

low-pressure region on the lee side, forming a typical conchoidally shaped hyporheic flow cell.

Upwelling GW is diverted around the hyporheic flow cell, mixes with SW, and then exits into

the overlying water from both sides, in patterns similar to those shown previously by Fox et al.

(2014) and Hester et al., (2019). SW and GW mixing zone (i.e. the mixing area where the

fraction of GW ranges between 16% and 84%) emerges as a thin band along the hyporheic flow

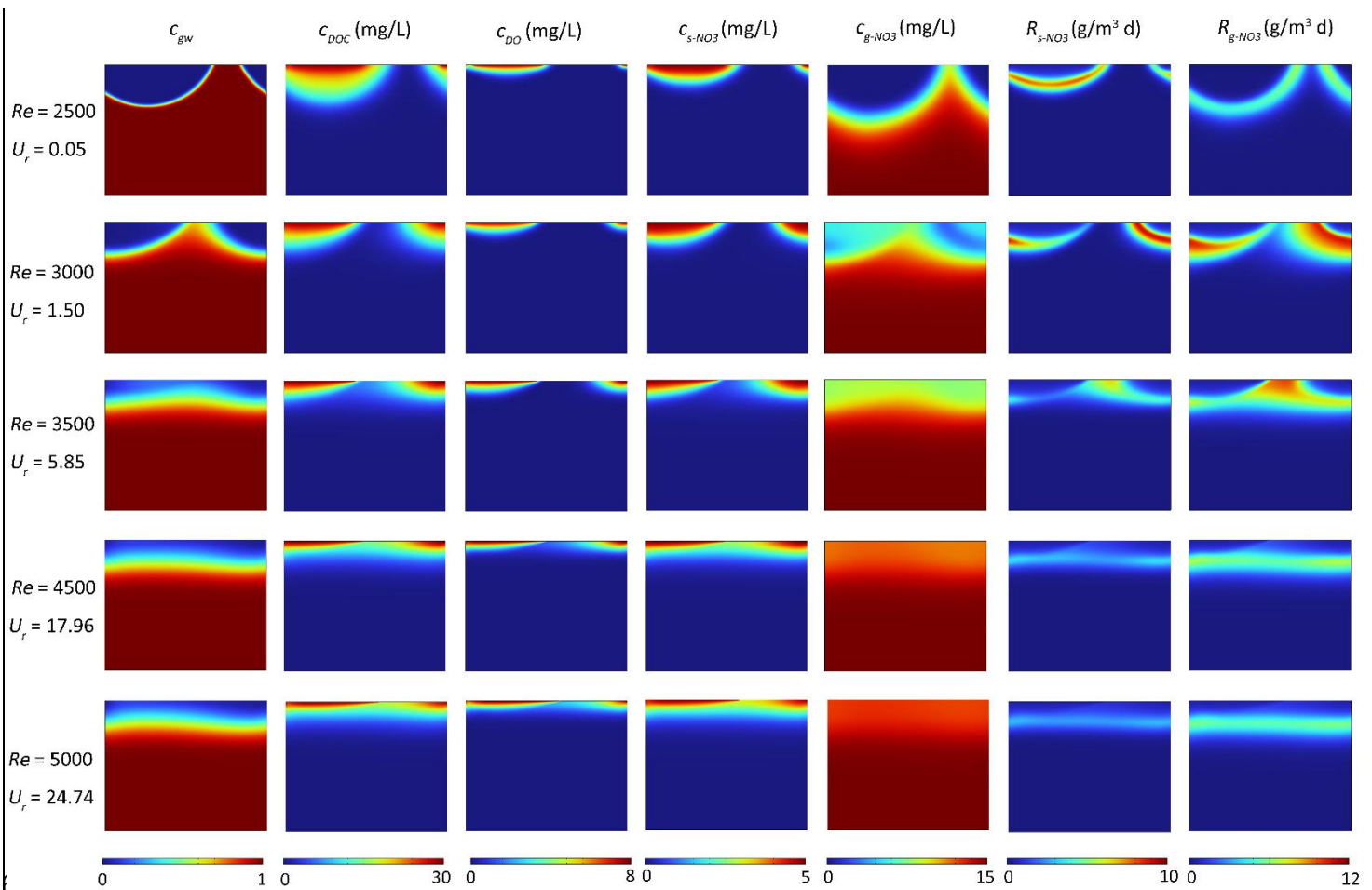cell, and covers over 2.978 % of the modeled domain. Meanwhile, NMD denitrification occurs

below the oxygen plume with the reactive zone in a conchoidal shaped distribution, while MD

denitrification reactive zone develops along the edge of the mixing zone, where DOC from SW

meets nitrate from GW (~~see~~ row 1 in Figure 4~~6~~).

At a surface water Re of 3000, bedforms migrate at a low celerity of 1.04 cm/h. This low

migration rate has minimal impact on the plumes of stream-borne O_2 and s-NO_3^-. The outflow

zone of groundwater-borne solutes (c_{gw} and g-NO_3^-) exhibits a slight upstream shift,

approaching the middle of the riverbed surface. The size of SW and GW mixing zone (GW

faction: 16%–84%) increases to 10.06% of the modeled domain. Furthermore, both the NMD

and MD denitrifying rates are enhanced at the start of bedform migration (row 2 in Figure 6).

~~As stream flow velocity increases ($Re = 3500$, $U = 0.175$ m/s), this changes the pressure~~

~~distribution patterns with its zones of high and low pressure. Consequently, the simulated~~

~~hyporheic flow cells move downstream, while simultaneously also shrinking in size. The shape~~

~~of the SW and GW mixing zone changes distinctly, forming a horizontal band with a wider~~

~~range 17.01% of the while domain. The penetration of stream-derived solutes into the streambed~~

~~is reduced, with a more gradual concentration gradient in the horizontal and vertical directions,~~

~~whereas the g-NO_3^- plume is uniformly distributed horizontally. Both NMD and MD~~

~~denitrification hot spots form in the central position near the sediment-water interface as the~~

~~bedform surface (see row 2 in Figure 4).~~

| | c_{gw} | c_{DOC} (mg/L) | c_{O2} (mg/L) | c_{s-NO3} (mg/L) | c_{g-NO3} (mg/L) | R_{s-NO3} (mg/L h) | R_{g-NO3} (mg/L h) |

$Re = 2500$, $U_r = 0.05$

$Re = 3500$, $U_r = 5.85$

$Re = 4500$, $U_r = 17.96$

$Re = 5000$, $U_r = 24.74$

Color scales: 0 – 0.5 – 1 | 0 – 15 – 30 | 0 – 4 – 8 | 0 – 2.5 – 5 | 0 – 7.5 – 15 | 0 – 0.2 – 0.4 | 0 – 0.2 – 0.4

Figure 46. Effect of bedform migration on riverbed biogeochemistry for $U_b = 0.6$ and $D_{50} =$
0.15 mm. Shown are profiles of (column 1) conservation solute representing groundwater
fraction (c_{gw}), (column 2) DOC concentration (c_{DOC}), (column 3) O_2 concentration (c_{O2}),
(column 4) s-NO_3^- concentration (c_{s-NO3-}), (column 5) g-NO_3^- concentration (c_{g-NO3-}), (column
6) non-mixing-dependent (NMD) denitrification rate (R_{s-NO3-}) and (column 7) mixing-dependent
(MD) denitrification rate (R_{g-NO3-}).

With increasing stream velocity ($Re = 3500$), bedform migration drives continuous changes
in pressure distribution. The simulated hyporheic flow cells move downstream and decrease in
size at the same time. The shape of the SW and GW mixing zone changes distinctly, forming a
horizontal band with a wider range 10.71~7.01% of the whole domain (GW faction: 16%–84%).

43

The penetration of stream-derived solutes into the streambed is reduced, with a more gradual

concentration gradient in the horizontal and vertical directions, whereas the g-NO$_3^-$ plume is

uniformly distributed horizontally. Both NMD and MD denitrification hot spots form in the

central position near the sediment-water interface as the bedform moving (row ~~2~~3 in Figure 6).

~~As stream flow velocity increases (*Re* = 3500, *U* = 0.175 m/s), this changes the pressure~~

~~distribution patterns with its zones of high and low pressure. Consequently, the simulated~~

~~hyporheic flow cells move downstream, while simultaneously also shrinking in size. The shape~~

~~of the SW and GW mixing zone changes distinctly, forming a horizontal band with a wider~~

~~range 17.01% of the while domain. The penetration of stream-derived solutes into the streambed~~

~~is reduced, with a more gradual concentration gradient in the horizontal and vertical directions,~~

~~whereas the g-NO$_3^-$ plume is uniformly distributed horizontally. Both NMD and MD~~

~~denitrification hot spots form in the central position near the sediment-water interface as the~~

~~bedform surface (see row 2 in Figure 4).~~

When bedform migration is further increased (*Re* = 4500~~*U$_r$* = 17.96~~ and 5000~~24.74~~), ~~the~~

bedform migration fully dominates over the pore water flow, and hence, continuous solute layers

are found in the subsurface (as depicted in row 4~~3~~ and 5~~4~~ of Figure 6~~4~~). The penetration depths

of stream-borne solutes are decreased in comparison to those in slow- to medium- fast migrating

bedforms. The NMD and MD denitrification zones become thin and move upward with

decreased reaction rates. Similar to the conclusions obtained in previous studies (Kessler et al.,

2015; Zheng et al., 2019), ~~the migration of the~~ bedform migration reduces the penetration depth

of solute and the scope of hyporheic exchange cell. We also found that bedform ~~a larger~~

migration ~~celerity~~ increases the size of mixing zone between surface water and groundwater.

The SW and GW mixing zone accounts for 9.30~~17.74~~% and 9.14~~17.86~~% of the domain area,

respectively (take the GW fraction 16%–84% for example).

**3.3 Effect of migration celerity on mixing regimes**

The mixing intensity across the riverbed~~bedform~~ surface and the size of the mixing area

within the subsurface were~~are~~ estimated by simulating four different grain sizes and five

upwelling ~~groundwater~~ GW fluxes, under varying stream velocities associated with the

corresponding bedform celerity. The evolutions of the hyporheic exchange flux, net mixing flux

and size of mixing zone with increasing Re number were~~are~~ summarized in Figure 5~~7~~. The 16–

84% GW fraction range was displayed here to evaluate how migration celerity affects mixing

regimes. ~~In the third row of Figure 5, *Fmix* represents the ratio of the net mixing flux to the total~~

~~hyporheic exchange flux. This total flux is triggered by both pumping and bedform migration,~~

~~and is simultaneously influenced by upwelling groundwater. *Fmix* serves as a metric to quantify~~

~~the proportion accounted for by the surface water-groundwater mixing flux within the overall~~

~~flux of surface water and groundwater interaction across the sediment-water interface.~~

~~As shown in Figure 5, the hyporheic exchange flux increases as the stream velocity and~~

~~bedform celerity rise across various grain sizes of the bedform, meanwhile the mixing flux~~

~~across the sediment-water interface also increases with the increasing stream velocity, except for~~

~~some special circumstances. For riverbed consists of very fine and fine sand (D_{50} = 0.08–0.15~~

~~mm) under moderate groundwater discharging conditions (U_b < 0.5), the mixing flux increases~~

~~significantly at the start of bedform migration, and then the mixing flux across the sediment-~~

~~water interface begins to decline with increasing celerity. In fact, this is because higher~~

~~migration velocities of a riverbed with relatively low permeability limits the discharge of~~

692 ~~groundwater into the river (a horizontal distribution of stream borne solute plume), leading to~~

693 ~~the mixing of SW and GW primarily occurring within the streambed (see the column 1 in Figure~~

694 ~~4). Concurrently, only the mixing flux through the water-sediment interface is reduced at this~~

695 ~~time.~~

696 ~~For medium sand (D_{50} = 0.22–0.36 mm), we found that the SW and GW mixing flux~~

697 ~~demonstrates a substantial increase relative to stationary bedforms when bedform migration~~

698 ~~initiates at moderate velocities. As migration celerity accelerates, the magnitude of mixing flux~~

699 ~~gradually approaches a plateau, with only marginal reductions observed at higher migration~~

700 ~~celerities. Besides, the size of SW and GW mixing zone also exhibit the similar trends.~~
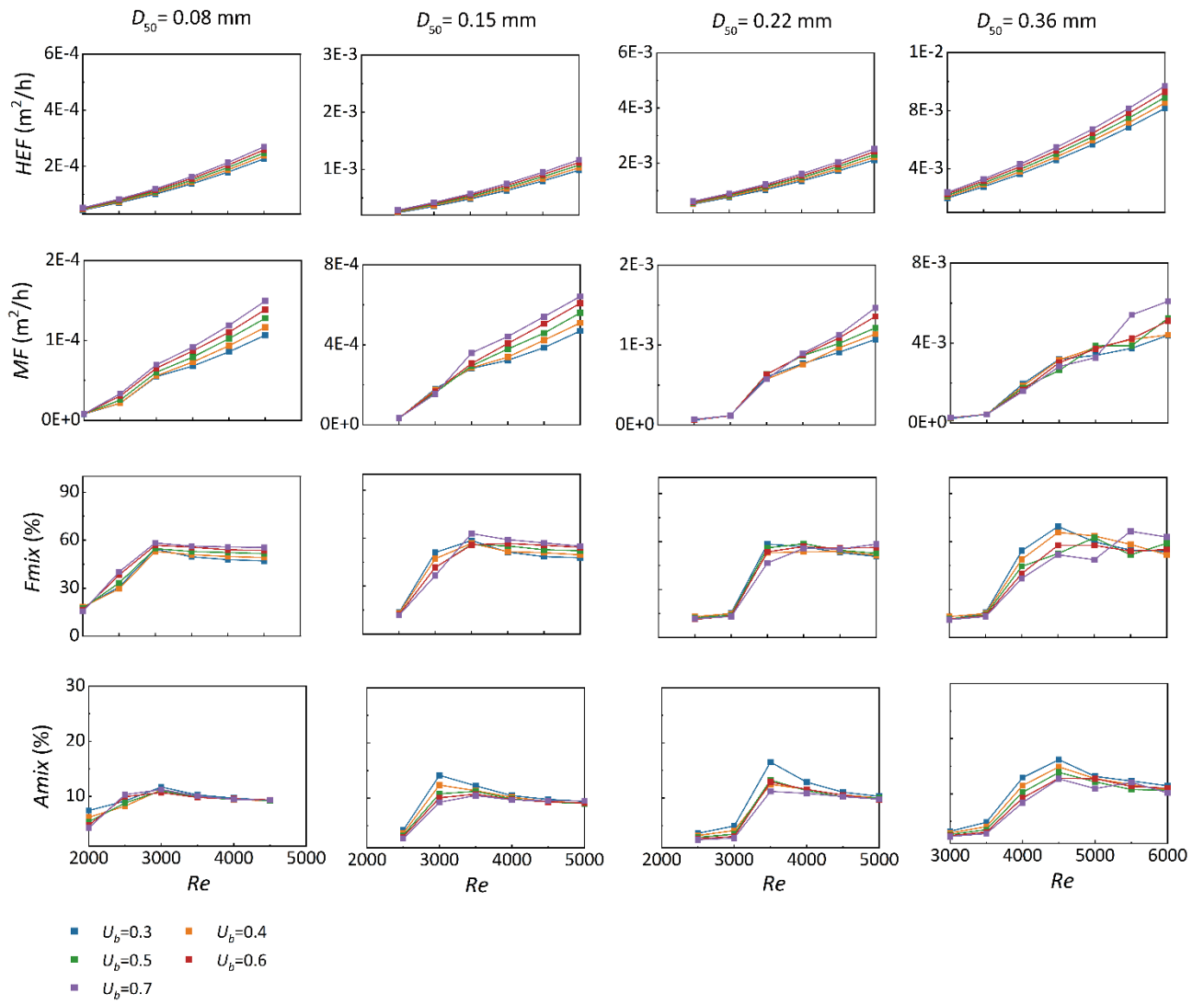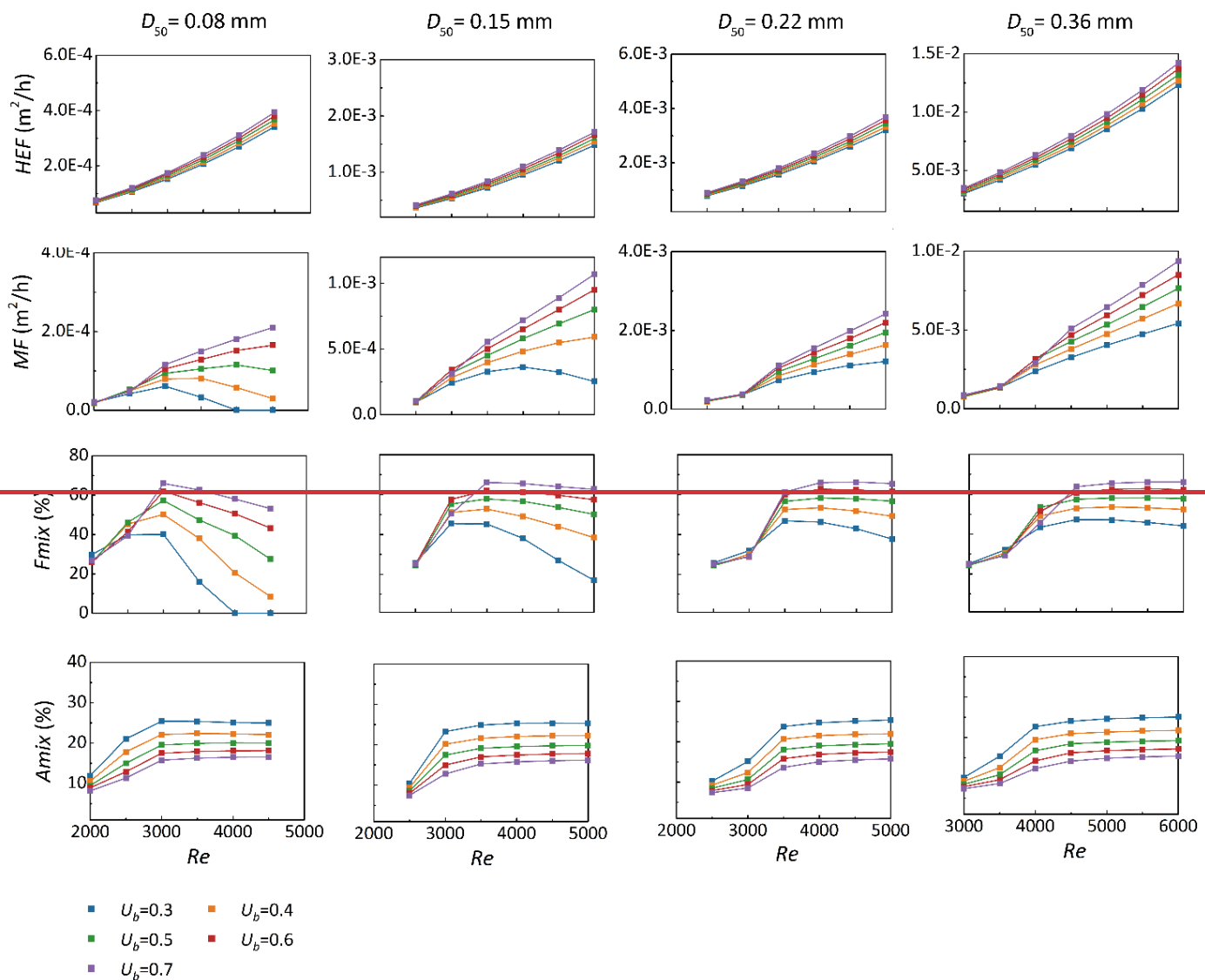
Figure 75. The variation of hyporheic exchange flux (*HEF*, row 1) and mixing flux (*MF*, row 2)

across the sediment-water interface, the proportion of mixing flux to hyporheic exchange flux

(*Fmix*, row 3) and the ratio ~~size~~ of mixing zone to whole domain (*Amix*, row 4) with stream

velocity and associated bedform celerity across different medium grain size when U_b = 0.3−0.7.

As shown in Figure 7, across various grain sizes, both *HEF* and *MF* increase with

increasing stream velocity and bedform celerity. Nevertheless, the mixing fraction exhibits a

significant increase at the onset of bedform migration, with a tendency to stabilize or decrease

48

moderately as celerity further increases. This phenomenon is attributed to enhanced mixing between SW and discharging GW along the entire horizontal riverbed in moving bedforms—contrasting with stationary bedforms, where mixing occurs solely along the typical crescent-shaped hyporheic exchange flow cells (Figure 6). Additionally, when bedforms start moving and move at moderate velocities, the SW-GW mixing zone shows a significant increase compared to stationary ones. As bedform migration celerity accelerates, the extent of the mixing zone gradually approaches a plateau, with slight reductions observed at higher celerities.

Although the GW fraction range determines both mixing flux and scope, it does not alter the effect of migration celerity on these mixing patterns. A broader groundwater fraction range induces a larger mixing flux, an increased *Fmix*, and a wider mixing zone; nonetheless, *Amix* persists as a relatively small scope (about 10–15% of the full domain) within the riverbed. Relatively moderate differences in computed *MF* and *Fmix* are observed between the narrower range (20–80%) and the baseline range (16–84%). For bedforms of different sediment grain sizes, *MF* represents around 60% of the total *HEF* when bedforms are moderately to fast-moving, compared with approximately 20% when they are stationary or slow-moving. Additionally, *Fmix* and *Amix* values obtained under various GW fraction ranges were presented in the Supporting Information (Text S4).~~Overall, bedform migration controls the shape and size of the SW and GW mixing zone, enhances the magnitude of hyporheic exchange flux and mixing flux. The mixing flux and size is also influenced by the upwelling GW flux. As U_b increases from 0.3 to 0.6, the mixing flux and the proportion of mixing flux to total hyporheic exchange flux rise significantly. An increase in U_b reduces the size of the mixing zone because both the hyporheic exchange flow cell and the mixing zone are confined to shallower depths~~
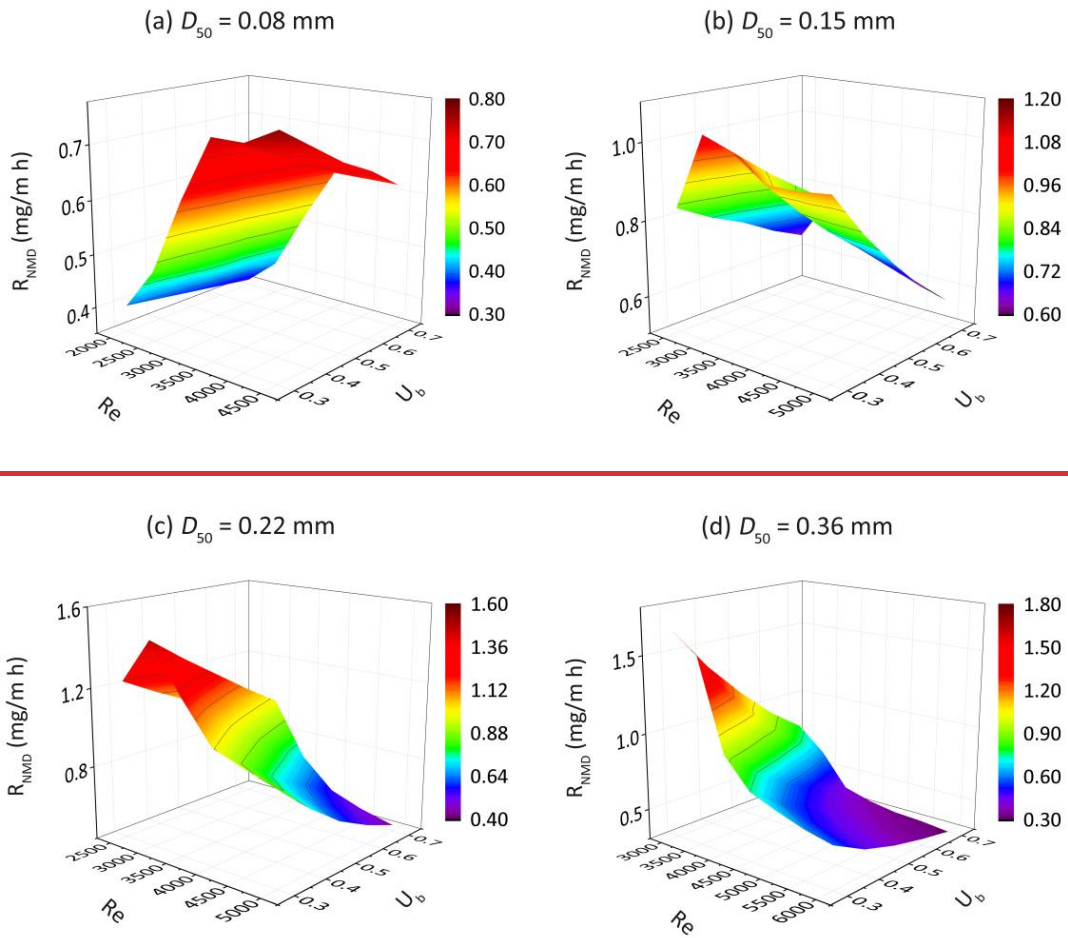
3.4 Impact of ripples migration on nitrate removal

To assess the impact of ripple migration on the removal of s-NO$_3^-$ and g-NO$_3^-$ within domains of varying medium grain sizes, the influx of nitrate into the riverbed layer and the total reaction rate within the riverbed layer were determined.

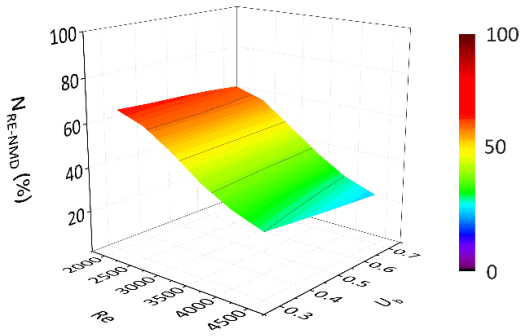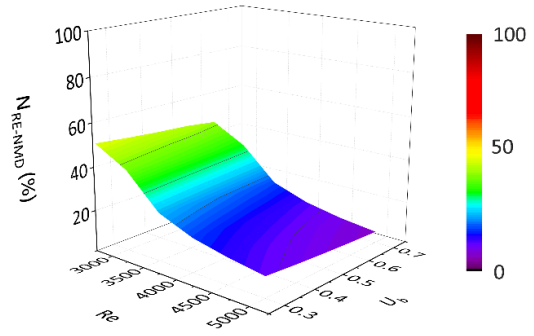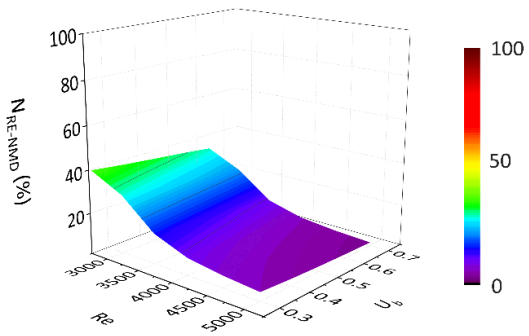(a) D_{50} = 0.08 mm (b) D_{50} = 0.15 mm (c) D_{50} = 0.22 mm (d) D_{50} = 0.36 mm
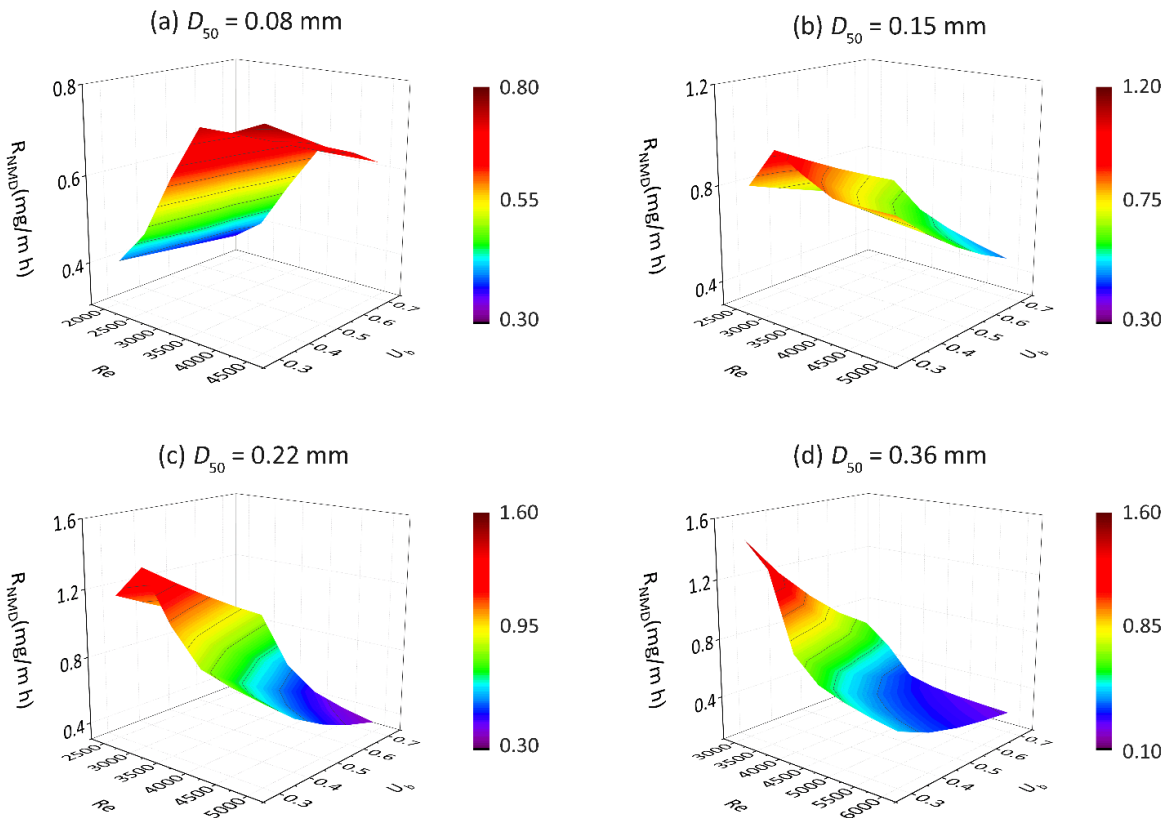
Figure 86. The non-mixing-dependent denitrification rates (R_{NMD}) as functions of U_b and Re for different medium grain sizes.
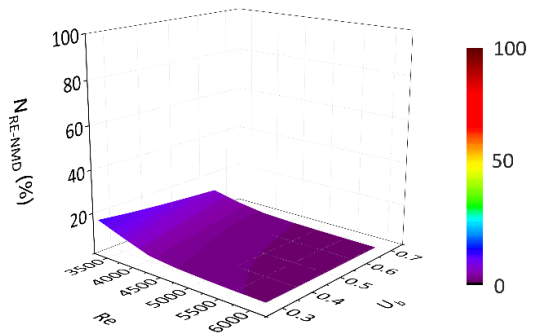
(a) D_{50} = 0.08 mm

(b) D_{50} = 0.15 mm

(c) D_{50} = 0.22 mm

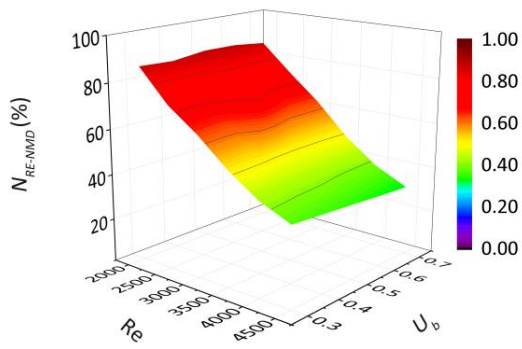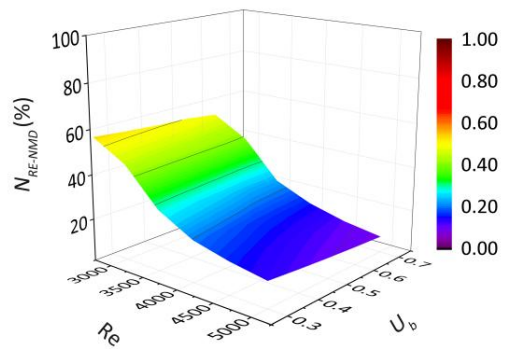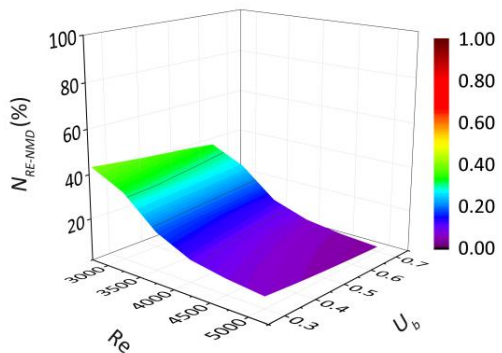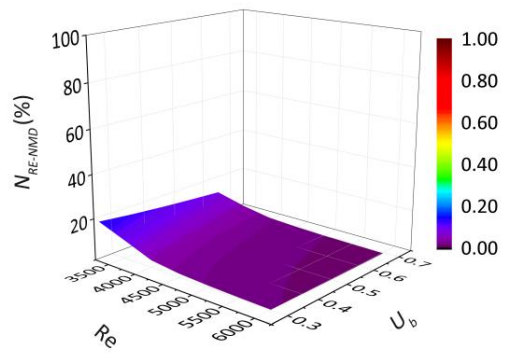(d) D_{50} = 0.36 mm

741

(a) D_{50} = 0.08 mm

(b) D_{50} = 0.15 mm

(c) D_{50} = 0.22 mm
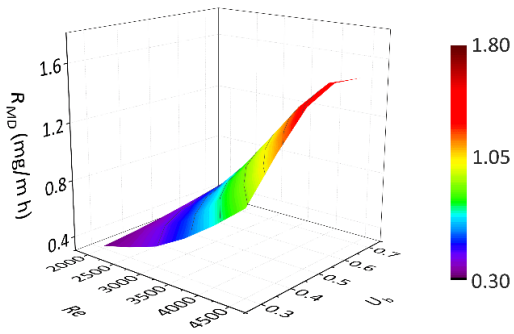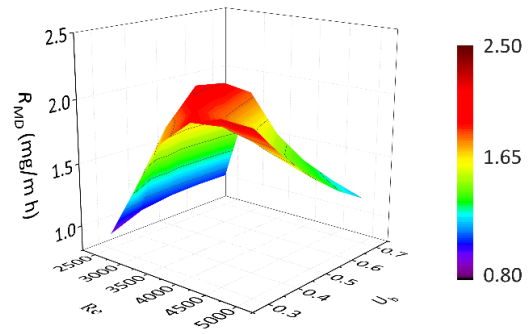
(d) D_{50} = 0.36 mm

742

743   **Figure 9~~7~~.** The removal efficiencies of stream borne nitrate ($N_{RE\text{-}NMD}$) as functions of U_b and Re

744   for different medium grain sizes.

745   For s-NO$_3^-$, the NMD denitrification rate increases <u>in moving bedforms</u> ~~with both the~~

746   ~~overlying water velocity and the migration celerity~~ <u>composed of</u>~~in~~ very fine sand ($D_{50} = 0.08$

747   mm). This is likely caused by higher flow velocities <u>driving more reactants into</u> ~~driving longer~~

748   ~~advective flow paths and increase solute residence times within~~ the sediment, thereby enhancing

749   denitrification in reaction-limited systems ($Da > 2.\underline{97}~~85~~$). In contrast, in riverbeds of fine to

750   medium sand ($D_{50} = 0.15{-}0.36$ mm) with higher permeabilities, the ~~reduction~~ rate of s-NO$_3^-$ is

751   negatively correlated with the mean stream velocity when the system becomes transport-limited

752   ($Da < 2$). This is likely because <u>s-NO$_3^-$</u>~~nitrate~~ travels fast along <u>shorten</u> flow paths and does not

753   undergo denitrification within the moving bedforms (Figure 6). Additionally, the migrating

754   bedforms enhance the delivery of s-NO$_3^-$ into the sediment due to increased <u> –HEF</u>~~hyporheic~~

755   ~~exchange flux~~. Consequently, the removal efficiency of s-NO$_3^-$ decreases monotonically across

756   various medium grain sizes (Figure 9~~7~~).
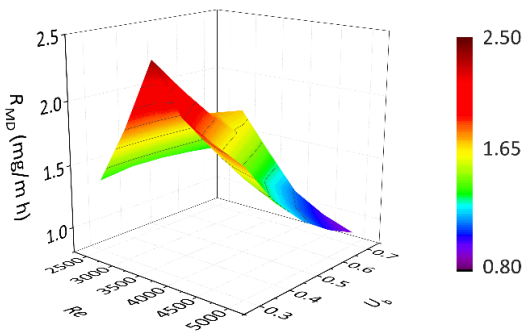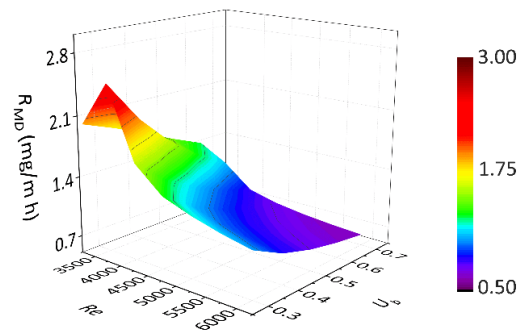
(a) D_{50} = 0.08 mm

(b) D_{50} = 0.15 mm
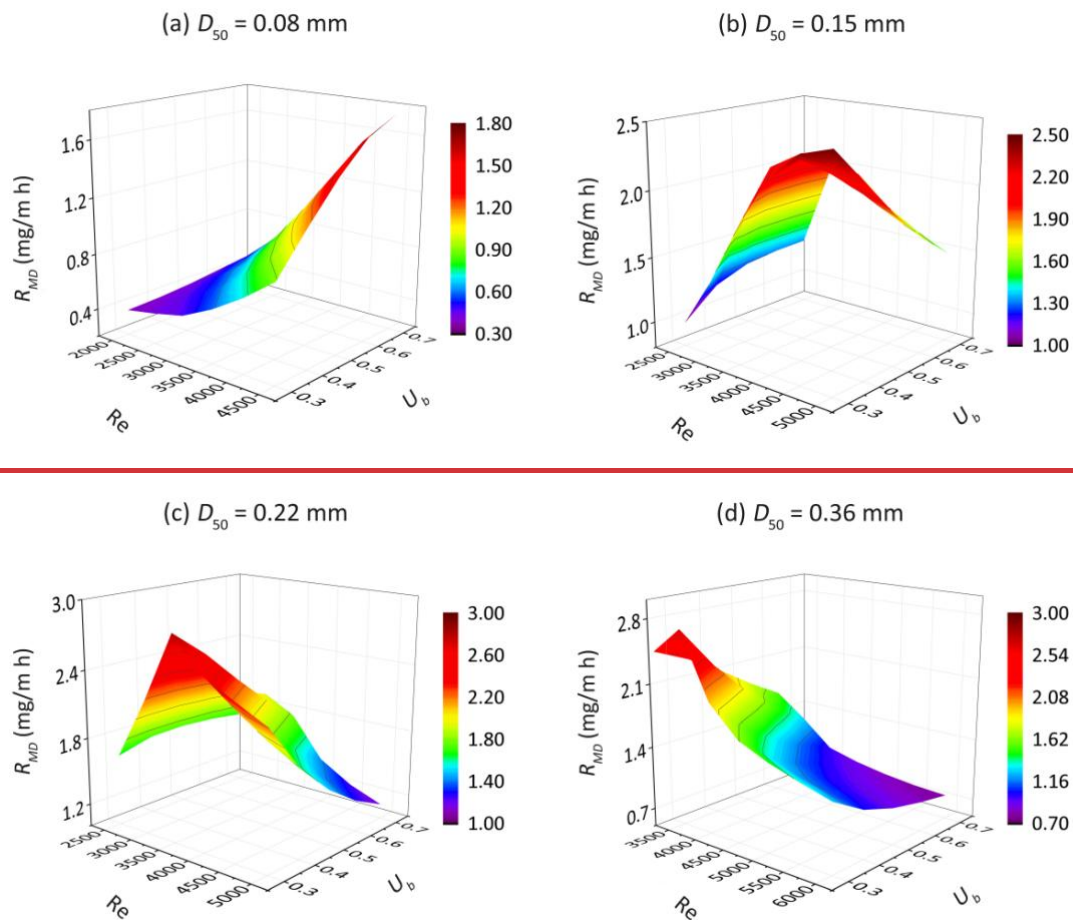
(c) D_{50} = 0.22 mm

(d) D_{50} = 0.36 mm

Figure 108. The mixing-dependent denitrification rates (R_{MD}) as functions of U_b and Re for different medium grain sizes.

For g-NO$_3^-$, the increase in MD denitrification is also seen for fine sandy sediments (D_{50} = 0.08−0.22 mm) g-NO$_3^-$ at low to medium Re when D_{50} < 0.36 mm (Figure 108). Compared to s-NO$_3^-$, the advective flow paths and residence times of g-NO$_3^-$ in groundwater are longer. Additionally, the enhanced mixing dynamics between SW and GW further facilitates the occurrence of MD denitrification as the bedforms start moving. Consequently, the reduction rate of g-NO$_3^-$ decreases only in riverbeds consisting of medium sand with fast bedform migration celerity (Re > 4000), as the solute residence time is significantly reduced. Interestingly, the rise in the MD denitrification rate compensates for the increased g-NO$_3^-$ nitrate influx in very fine sand (D_{50} = 0.08 and 0.15 mm) at moderate high stream velocity (Re < 4000). Most of g-NO$_3^-$

770   that enters the sediment is consumed before entering the overlying water column. For fine to

771   medium sand riverbed ~~(D_{50} = 0.15–0.36 mm)~~, the g-NO$_3^-$ removal efficiency decreases strongly

772   with increasing Re. The natural protective role of the SW and GW mixing zone in preventing

773   nitrate-contaminated <u>GW</u> ~~groundwater~~ from entering rivers is being hindered <u>in fast moving</u>

774   <u>bedforms</u> (Figure ~~9~~11).

(a) D_{50} = 0.08 mm   (b) D_{50} = 0.15 mm

(c) D_{50} = 0.22 mm   (d) D_{50} = 0.36 mm

775
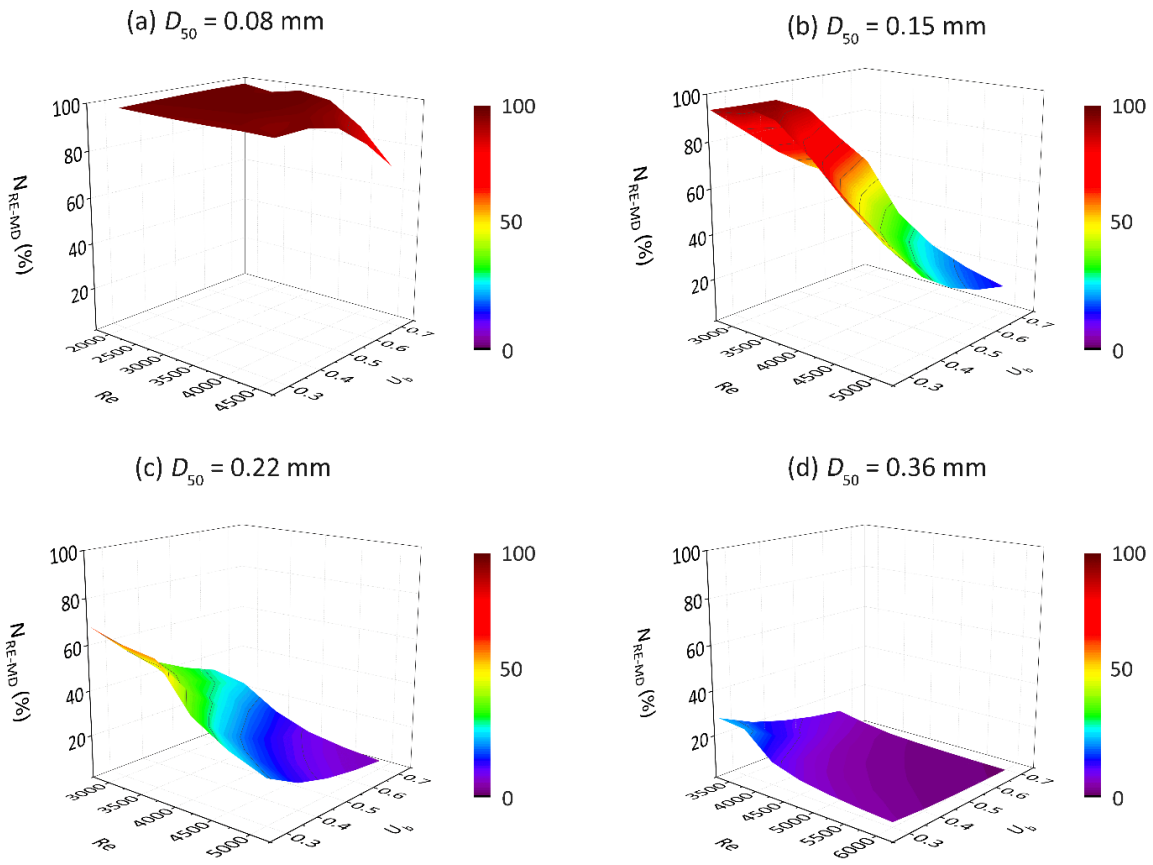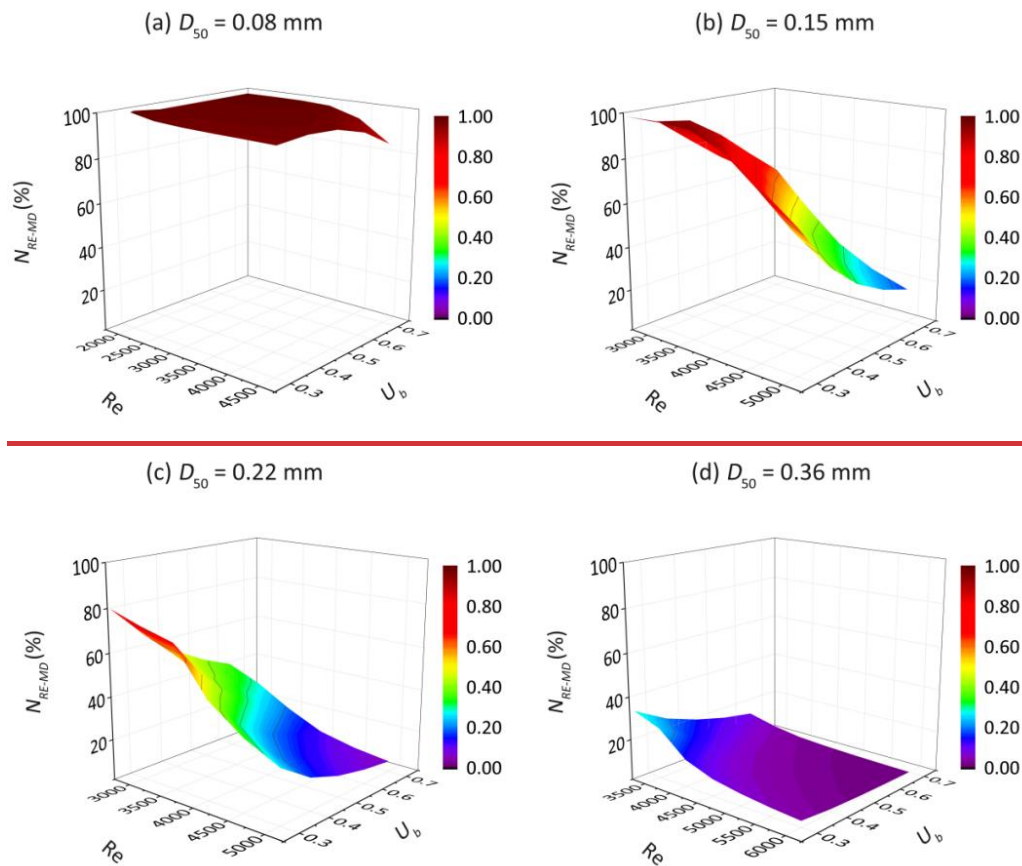
Figure 119. The removal efficiencies of groundwater borne nitrate (N_{RE-MD}) as functions of U_b and Re for different medium grain sizes.

4. Discussion

This study for the first time quantified the effect of bedform migration on surface waterSW and groundwater GW mixing process as well as mixing triggered denitrification. Previous research has primarily focused on the potential impacts of bedform migration on hyporheic exchange driven by streambed morphological features, as well as non-mixing-dependent biogeochemical processes where reactants are assumed to be reside predominantly in

SWsurface water. However, such studies represent only a small subset of possible streambed environmental conditions, focusing exclusively on specific headwater stream conditions (Jiang et al., 2022; Kessler et al., 2015; Ping et al., 2022; Zheng et al., 2019). The impact of bedform

788 migration on the conceptual model of bedform-induced hyporheic exchange, which is

789 influenced by ~~groundwater~~ GW upwelling and/or ambient lateral ~~groundwater~~ GW flow in the

790 mid-stream section of lowland rivers, has received relatively less attention and examination.

791 In streams and rivers that are fed by regional ~~groundwater a~~GW and possess undulating

792 bedforms, SW ~~surface water~~ gets mixed with ~~groundwater~~ GW throughout the local hyporheic

793 exchange process. The mixing zone exhibits a typical crescent shape along the periphery of

794 typical hyporheic exchange cells within a stationary streambed (as reported by Fox et al., 2014;

795 Hester et al., 2019; Nogueira et al., 2022). The sizes of the ~~surface water~~SW-~~groundwater~~ GW

796 mixing zone (e.g., thickness and area) occupy a small proportion of the whole HZ. In the

797 immobile bedform, the thin mixing zone~~s (16 ~ 84% ranges)~~ occupying ~5~~10~~% is consistent

798 with prior work (Hester et al., 2013; Santizo et al., 2020). However, at the onset of bedform

799 migration, the mixing pattern, extent, and intensity of SW-GW interactions are altered. ~~During~~

800 ~~the initiation of bedform migration, however, the mixing pattern, size, and intensity of surface~~

801 ~~water-groundwater interactions undergo modification.~~ A continuous SW-GW mixing zone is

802 formed within the ripples of the medium- to fast-moving bedform (Figure 6~~4~~), and the area of

803 mixing zone increases to approximately 10 ~~15~~~ 15~~25~~% at this time. Besides, the net flux of

804 ~~surface water~~SW and GW~~groundwater~~ mixing ~~across the sediment-water interface (or within the~~

805 ~~riverbed) is also~~ increase~~s~~d with stream velocity and bedform migration celerity significantly

806 (Figure 7~~5~~). As a result, bedform migration controls and determines the hotspots and magnitudes

807 of the SW and GW mixing. The bedforms are typically assumed to be immobile potentially

808 making underestimations of SW~~surface water~~-GW ~~and groundwater~~ mixing flux and mixing

809 zone in a HZ.

810   Instead of the typical crescent-shaped ~~mixing-dependent~~ (MD~~)~~ denitrifying zone observed

811   in stationary bedforms (Naranjo et al., 2015; Hester et al., 2014, 2019), the MD reaction

812   zonation changes to the layer shape distributed at the fringe of the HEF cells, where mixing

813   between SW and GW develop to a largest degree (Figure _–6<u>5</u>). Such a situation exists where the

814   stream flows into with a relative homogeneous sandy riverbed with low autochthonous organic

815   carbon content and encounters with nitrate enrich–_ <u>GW</u>~~groundwater~~. The heterogeneous

816   streambeds including buried autochthonous organic matter (Sawyer, 2015; Ping et al., 2022),

817   deposited particulate organic particles (Drummond et al., 2017; Ping et al., 2023), and biological

818   aggregate (Xian et al., 2022), would complicate the hyporheic exchange process, induce the

819   rough and irregular shapes and boundaries of HEF cells and mixing zone, and therefore affect

820   redox microenvironments and biogeochemical zonations. MD denitrifying hotspot would also

821   <u>develop</u>~~occur~~ around available sources of DOC.

In panel (a):
$Da=0.397+0.828*0.589^{Ur}$
$(R^2=0.90)$

$Da=0.101+0.232*0.490^{Ur}$
$(R^2=0.94)$

$D_{50}=0.36$ mm
$D_{50}=0.22$ mm

In panel (b):
$Da=3.919+9.81*0.886^{Ur}$
$(R^2=0.86)$

$Da=0.849+1.950*0.801^{Ur}$
$(R^2=0.95)$

$D_{50}=0.15$ mm
$D_{50}=0.08$ mm
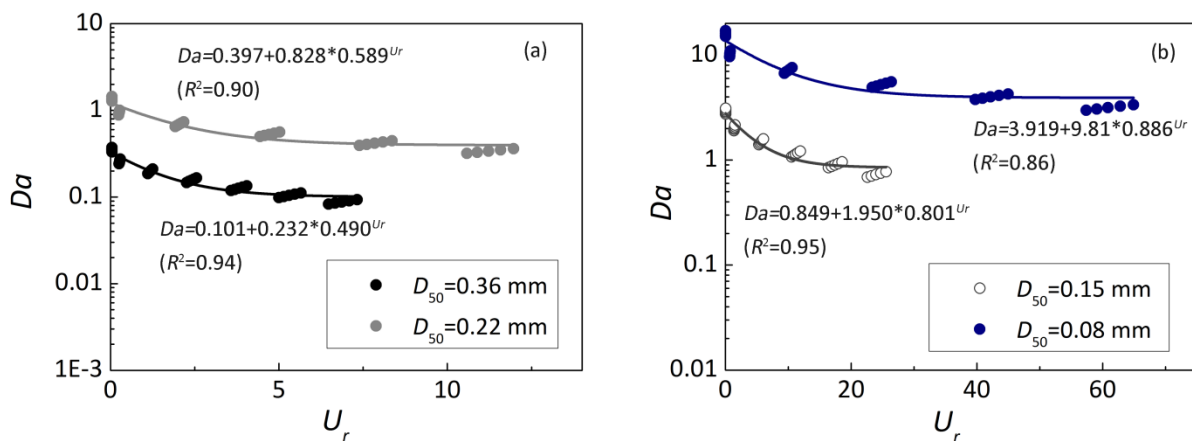
823   **Figure 1<u>0</u>2.** Variation of the dimensionless Damköhler number as a function of the

824   dimensionless parameter U_r.

825   Previous studies have demonstrated that migrating bedforms constrains the penetration

826   depths of stream-borne solute<u>, shorten their transport timescale,</u> and reduces the removal

827   efficiency of stream-borne nitrate (Jiang et al., 2022; Kessler et al., 2015; Ping et al., 2022;

828   Zheng et al., 2019). Our findings indicate that bedform migration exerts more complex

829   influences on MD denitrification and groundwater-borne nitrate removal. Bedform migration

830   facilitates increases in the MD denitrification rate, driven by enhanced mixing flux, a higher

831   mixing proportion, and an expanded mixing zone. At the same time, it shortens the residence

832   timescale of water and solutes, which is detrimental to the occurrence of denitrification. When

833   $Re < 4000$ (slow to moderate stream velocities), the MD denitrification rate of moving bedforms

834   is greater than or comparable to that of stationary bedforms; in contrast, for fast-moving

835   bedforms ($Re \geq 4000$), the MD denitrification rate decreases significantly. This is likely because

836   the reduction in MD rate driven by a shortened transport timescale dominates over the increase

837   caused by enhanced mixing intensity; meanwhile, at this stage ($\sim Re$ 4000), the mixing fraction

838   of the total exchange flux and the extent of the mixing zone both approach plateaus. Fast-

839   moving bedforms also reduce the HZ attenuation capacity for groundwater-borne nitrate.

840   Notably, the g-NO_3^- removal efficiency in HZs peaks for stationary bedforms and those at the

841   onset of migration.

842   ~~Our results revealed that the bedform migration also reduces the HZ attenuation ability for~~

843   ~~groundwater borne nitrate.~~ The causes of fast-moving bedforms' negative impact on g-NO_3^-

844   removal differ depending on the type of riverbed sediment~~However, the reasons for this~~

845   ~~phenomenon are different for various riverbed sediments~~. For very fine sand ($D_{50} = 0.08$ mm), a

846   larger celerity results in a decline in transport timescale with less impact on removal efficiency

847   as the system is rate-limited ($Da \gg 1$). For fine to medium sand riverbed ($D_{50} = 0.15–0.36$

848   mm), the transport-limited situation leads to a low denitrification rate with increasing U_r but

849 constantly decreasing *Da* (*Da* < 1). It is important to note that the ~~calculated~~ reaction timescale

850 ~~we calculated~~ is based on the consumption period of oxygen to a prescribed anoxic threshold.

851 Under these conditions, the exhaustion of labile DOC would also lead to the cessation of

852 denitrification (Zarnetske et al., 2011a, 2011b). These results demonstrate that in order to

853 evaluate the self-purification capacity of the HZ and its function as a natural barrier mitigating

854 groundwater contamination, riverbed sediment transport dynamics and grain size distributions

855 need to be considered. Stabilizing bedform configurations in restoration projects would enhance

856 the natural attenuation capacity of HZs. Additionally, enhancing mixing intensity, along with

857 extending the water residence timescale, would also facilitate the self-purification of

858 HZs.~~Stabilizing bedform configurations in restoration projects would enhances the natural~~

859 ~~attenuation capacity of the HZ.~~

860 Different from previous studies that demonstrated the magnitude of NMD denitrification

861 is~~was~~ often greater than that of MD denitrification (Hester et al., 2014; Trauth and Fleckenstein,

862 2017). The results in our study show that the total reaction rate of s-NO_3^- is~~was~~ smaller than that

863 of g-NO_3^- in mobile bedforms. This phenomenon can be attributed to the following two reasons:

864 First, the concentration of s-NO_3^- is one-third that of g-NO_3^-; Second, the reaction zone is

865 reduced by migration celerity for NMD denitrification, while the reaction zone for MD

866 denitrification is increased in the moving riverbed ~~at the onset of bedform migration~~. Mixing

867 intensity increases with bedform migration, a process that facilitates MD denitrification more

868 effectively~~The mixing intensity increases with bedform migration, which facilitates the MD~~

869 ~~denitrification more effectively~~ (Hester et al., 2019; Nogueira et al., 2024; Trauth and

870 Fleckenstein., 2017). ~~Moreover, migration celerity increases the influx of nitrate into the HZ by~~

871 ~~enhanced hyporheic exchange, while it has less impact on upwelling GW flux. Hence, the~~

872 ~~removal efficiency of g-NO$_3^=$ is also higher than that of s-NO$_3^=$ in these scenarios.~~ More

873 attention should be paid to the mixing dynamics and mixing triggered biogeochemical reactions,

874 which is helpful to put forward appropriate stream restoration plans so as to enhance the health

875 of the aquatic ecosystem (Hester et al., 2017; Lawrence et al., 2013).

876 The findings of this study, derived from 2D numerical models, are most directly

877 generalizable to straight, low-curvature streams with periodic bedform distributions in riverbed

878 sediments. In such stream systems, hyporheic exchange is dominated by streamwise-vertical

879 flow cells, with lateral (cross-stream) hyporheic flux accounting for a small fraction of total

880 exchange (Hu et al., 2014; Naranjo et al., 2015). Importantly, straight, low-curvature streams are

881 prevalent in agricultural and urban downstream gaining reaches, which are characterized by

882 relatively homogeneous sediment types (e.g., fine sands). This is consistent with the focus of our

883 study, as these reaches often face nitrate pollution challenges and depend on natural attenuation

884 to maintain water quality (Hester et al., 2014; Trauth et al., 2017). In practice, riverbeds may

885 exhibit far more complex three-dimensional (3D) bedform morphologies coupled with sediment

886 heterogeneity, for example, in highly meandering streams (Gomez-Velez et al., 2017; Nogueira

887 et al., 2024; Pescimoro et al., 2019). Future studies should establish 3D numerical model and

888 incorporate stochastic hydraulic conductivity (K) fields to explore how sediment heterogeneity

889 interacts with bedform migration, evaluating whether high-K hotspots enhance or reduce

890 migration-driven mixing.

891 A critical limitation of this study is the reliance on empirical equations for bedform

892 migration celerity. The Chezy equation (suited for flat, homogeneous sediment beds) was used

to estimate the shear velocity for incipient sediment motion, with the experimentally derived empirical relationship by Coleman and Melville (1994) further adopted to account for the additional shear stress induced by ripples. The two-step approach (shear stress for particle initiation and ripple-scale form drag via empirical formulations) reproduced Wolke's (2020) results and proved useful for investigating the effects of bedform migration on hyporheic solute transport (Ahmerkamp et al., 2017; Zheng et al., 2019). We did not simulate turbulent flow over triangular bedforms nor compute shear stress via computational fluid dynamics (CFD; a numerical method that would yield more precise pressure profiles and shear stress distributions) given that the core focus of this study was to investigate how bedform migration affects hyporheic solute transport and mixing-dependent denitrification within the riverbed layer. As future work, the empirical approach should be validated using CFD simulations to enhance the accuracy of bedform-related stress and migration calculations. This validation will facilitate the quantification of potential uncertainties and refine the mechanistic understanding of bedform dynamic-hyporheic zone interactions.

This study focuses on ripples and, more broadly, shorter-wavelength topographic roughness elements formed under low subcritical flow conditions in sandy riverbeds (Ashley, 1990; Gomez-Velez et al., 2015; Raudkivi, 1997). The undulating bedforms maintain dynamic equilibrium through geometric adjustments, with their geometry remaining unchanged as the stream velocity fluctuates within a specific range (10–30 cm/s). When stream velocities exceed this upper threshold, a condition commonly observed in fast-flowing rivers, bedform geometries can be altered, ultimately leading to bedform erosion (Boano et al., 2013; Harvey et al., 2012). This process is not accounted for in the current model. If small-scale ripples develop and merge

with larger-scale ripples and dunes under high stream velocities, the removal efficiency of s-NO_3^- and g-NO_3^- may be enhanced due to the extended hyporheic flow paths and increased residence timescales (Harvey et al., 2012; Zomer and Hoitink, 2024). Otherwise, the removal of s-NO_3^- would be highly hindered because of shorter residence time and fully oxic condition in fast moving bedforms and fast flowing rivers, while the removal of g-NO_3^- would likely be less affected within the immobile streambeds.

The numerical models assume isotropic sediment K. In fact, natural riverbeds with small-scale bedforms (e.g., dunes and ripples) commonly exhibit strong anisotropy. For bedforms with flow-transverse crests, pore pathways parallel to the crests are relatively continuous and straight yielding high transverse K. In contrast, pathways perpendicular to the crests are highly tortuous: water here must move upward through erosional, high-porosity troughs and downward over depositional, low-porosity crests. This undulating flow path, combined with flow separation and local energy losses at morphological transitions, substantially increases hydraulic resistance and lowers longitudinal K (Dallmann et al., 2020; Salehin et al., 2004). Additionally, spatial variability in bedform dimensions (e.g., increasing dune wavelength downstream) enhances this anisotropy by introducing zones of differing flow resistance along the streamwise direction (Venditti et al., 2005). Given that the model is constructed along a longitudinal section with spatially consistent, periodic bedforms, the use of an isotropic hydraulic conductivity assumption is justified. Incorporating anisotropic K is critical for accurately modeling hyporheic exchange and related biogeochemical processes in 3D heterogeneous models.

In this study, we focused on ripples and, more broadly, shorter-wavelength topographic roughness elements that form under low subcritical flow conditions in sandy riverbeds (Ashley,

1990; Gomez-Velez et al., 2015; Raudkivi, 1997). The undulating bedforms maintain dynamic equilibrium through geometric adjustments, with their geometry remaining unchanged as the stream velocity fluctuates within a specific range (10–30 cm/s). When stream velocities exceed this upper threshold, a condition commonly observed in fast-flowing rivers, bedform geometries can be altered, ultimately leading to bedform erosion (Boano et al., 2013; Harvey et al., 2012). This process is not accounted for in the current model. If small-scale ripples develop and merge with larger-scale ripples and dunes under moderate stream velocities, the removal efficiency of s-NO_3^- and g-NO_3^- may be enhanced due to the extended hyporheic flow paths and increased residence timescales (Harvey et al., 2012; Zomer and Hoitink, 2024). Otherwise, the removal of s-NO_3^- would be highly hindered because of shorter residence time and fully oxic condition in fast-moving bedforms and fast-flowing rivers, while the removal of g-NO_3^- would likely be less affected within the immobile streambeds.

In our model, dissimilatory nitrate reduction to ammonium (DNRA) was not incorporated in the model, given that denitrification is typically regarded as the predominant pathway for nitrate removal, whereas DNRA plays a secondary role in nitrate transformation (Zarnetske et al., 2012). Lansdown et al. (2012) and Quick et al. (2016) have demonstrated that approximately 5% of $^{15}NO_3^-$ tracer in river sediment incubations underwent DNRA, while 85% underwent denitrification. Nevertheless, DNRA competes with denitrification for NO_3^- and DOC as electron acceptor and donors within HZs. When an oligotrophic and/or a pristine stream infiltrate into the streambed and subsequently interact and mix with nitrate-enriched GWgroundwater, the MD DNRA would not occur due to the low C/N ratio. MD denitrification zone shifts upstream toward the overlying water column, leading to a pronounced spatial

959 ~~mismatch between the denitrification zone and the mixing interface. This occurs because DOC~~

960 ~~is intensively consumed within the HEF cell, such that elevated MD denitrification rates emerge~~

961 ~~below the DOC and oxygen plumes yet above the mixing zone. Specifically, this phenomenon~~

962 ~~can be attributed to the critical role of dispersion effect in solute transport and mixing-triggered~~

963 ~~denitrification, besides advection effect.~~ When ~~an~~a eutrophication stream with higher DOC

964 concentration, DNRA would have a greater influence in nitrate transformation because DNRA is

965 prone to occur in NO_3^--limited (that is DOC sufficient) conditions compared to denitrification

966 (Zhu et al., 2023). The ammonia produced by MD ~~mixing-dependent~~ DNRA would be further

967 nitrified within the aerobic HEF cell, thereby potentially elevating the risk of nitrate pollution in

968 SW~~surface water~~.

969   In this~~our~~ model, stream velocity and upward GW ~~groundwater~~ flux are considered

970 constant in the present model, yet they may change in time due to storm events, tidal pumping,

971 snowmelt, or reservoir hydro-peaking (Liu et al., 2024; Nogueira et al., 2022; Song et al., 2018).

972 Hester et al. (2019) demonstrated that increasing surface water stage would enhance both NMD

973 and MD denitrification. Nogueira et al. (2024) and Trauth and Fleckenstein (2017) pointed out

974 that GW ~~groundwater~~ discharge events increase the magnitude of SW~~surface water~~-

975 GW~~groundwater~~ mixing, therefore effecting the prevalence of MD denitrification. The

976 interactions among morphological dynamics, hyporheic exchange, and biogeochemical

977 processes under transient conditions are key areas for future research.

5. Conclusion

The numerical model developed in this study was used~~applied~~ to simulate the interaction and mixing of upwelling groundwater with bedform-induced hyporheic flow, examining how bedform migration influences ~~surface water~~SW and ~~groundwater~~ GW mixing and the processing of groundwater-borne nitrate within the HZ. Our analysis quantified the mixing flux and the size of mixing zone, as well as the mixing-dependent denitrification rates and removal efficiencies across riverbed sediments characterized by varying grain sizes, stream flow velocities, and groundwater discharge fluxes. These model simulations reveal~~ed~~ that as bedforms migrate, the SW~~surface water~~-GW~~groundwater~~ mixing zone and the associated mixing-dependent denitrification zone progressively evolve into uniform, band-like structures. When turnover dominates the hyporheic exchange process, the mixing flux increases significantly (an increase of one order of magnitude). The mixing proportion of total exchange flux and mixing zone scope also experience significant increases at the onset of migration; as stream velocity further rises, the mixing proportion (~60%) and mixing size (~10–15% of the riverbed) gradually reach plateaus. Enhanced SW-GW mixing dynamics facilitates MD denitrification as bedforms begins migration; however, shortened solute residence timescales resulting from fast bedform movement limits MD denitrification occurrence.~~For riverbeds composed of fine to medium sand~~ ~~(D_{50} = 0.15–0.36 mm), both the magnitudes of SW and GW exchange flux and mixing flux~~ ~~increase significantly when turnover becomes the dominant exchange mechanism, while the~~ ~~proportion of mixing flux across the sediment-water interface and the size of mixing zone~~ ~~remain approximately constant at this time. Meanwhile, both the mixing-dependent~~ ~~denitrification rates and removal efficiencies decline significantly with increasing stream flow~~

1000 ~~velocities and associated bedform migration rates.~~ Under dynamic bedform conditions, the

1001 self-purification capacity of the HZ is reduced for fine to medium sand (D_{50} = 0.15–0.36 mm),

1002 compromising its role as a natural barrier against groundwater contamination. Incorporating the

1003 identified and analyzed factors can enhance the management of riverbed sediment-associated

1004 aquatic systems, particularly for management objectives focused on removing groundwater-

1005 borne nitrate.~~The management of aquatic systems involving riverbed sediments can be enhanced~~

1006 ~~by incorporating the analyzed factors identified here, particularly when management goals~~

1007 ~~encompass the removal of groundwater borne nitrate.~~

1008

1009 ~~Notation~~

~~S~~   ~~Stream slope [-]~~

~~H~~   ~~Water depth [L]~~

~~U~~   ~~Stream velocity [L T^{-1}]~~

~~λ~~   ~~Ripple wavelength [L]~~

~~u_c~~   ~~Bedform migration celerity [L T^{-1}]~~

~~l~~   ~~Streambed height [L]~~

~~H_d~~   ~~Ripple height [L]~~

~~D_{50}~~   ~~Median sediment size [L]~~

~~x~~   ~~Horizontal coordinate, rightward positive [-]~~

~~y~~   ~~Vertical coordinate, upward positive [-]~~

~~k~~   ~~Sediment permeability [L^2]~~

K	Sediment hydraulic conductivity [L T^{-1}]
h	Hydraulic head [L]
h_m	Amplitude of the sinusoidal head variation [L]
m	Wavenumber of the variation [-]
g	Gravity acceleration [L T^{-2}]
c_i	Concentration of reactive components [M L^{-3}]
c_{gw}	Groundwater tracer [M L^{-3}]
v	Seepage velocity [L T^{-1}]
θ	Sediment porosity [-]
α_L	Longitudinal dispersivities
α_T	Transverse dispersivities [L]
D_{ij}	Hydrodynamic dispersion [L^2 T^{-1}]
D_m	Molecular diffusion coefficient [L^2 T^{-1}]
τ	Tortuosity factor [-]
V_{AR}	Maximum reaction rate of aerobic respiration [T^{-1}]
V_{DN}	Maximum reaction rate of denitrification [T^{-1}]
K_{inh}	Non-competitive inhibition factor [M L^{-3}]
K_{DOC}	Half-saturation for dissolved organic carbon [M L^{-3}]
K_{NO3^-}	Half-saturation for nitrate [M L^{-3}]
K_{O2}	Half-saturation for oxygen [M L^{-3}]
X_{AR}	Microbial concentration facilitating aerobic respiration [M L^{-3}]
X_{DN}	Microbial concentration facilitating denitrification [M L^{-3}]

ρ_s Sediment density [M L^{-3}]

ρ Water density [M L^{-3}]

P Hydraulic pressure [M L^{-1}T^{-2}]

u^* Bed shear velocity [L T^{-1}]

u_{cr}^* Critical bed shear velocity [L T^{-1}]

n Manning coefficient [-]

τ^* Shield parameter [-]

τ_{cr} Critical shear stress [M L^{-1}T^{-2}]

τ_{cr}^* Critical Shield parameter [-]

r Submerged specific gravity of sediment [-]

R_{O2} Aerobic respiration rate [M L^{-3}T^{-1}]

$R_{s\text{-}NO3}$ Non-mixing-dependent denitrification rate [M L^{-3}T^{-1}]

$R_{g\text{-}NO3}$ Mixing-dependent denitrification rate [M L^{-3}T^{-1}]

R_{DOC} Dissolved oxygen carbon consumption rate [M L^{-3}T^{-1}]

υ Kinematic viscosity of water [L^2 T^{-1}]

u_s Underflow seepage velocity induced by stream gradient [L T^{-1}]

Re Reynolds number [-]

U_r ratio of bedform celerity to pore water velocity [-]

u_p Darcy velocity induced by pumping process [L T^{-1}]

u_q Vertical groundwater flux [L T^{-1}]

U_b Ratio of vertical groundwater flux to hyporheic exchange flux

τ_R Biogeochemical reaction timescale [T]

τ_T	Water transport timescale [T]
Da	Damköhler number [-]
Δx	Bedform migrating displacement per timestep (L)
dt	The length of per timestep (T)
Da'	Conversion factor for unit Darcy to m^2 [-]
F_{mix}	the proportion of mixing flux to hyporheic exchange flux [-]
A_{mix}	Surface water and groundwater mixing zone [L^2]
A	Streambed area [L^2]
M_{NDN}	Nitrate removed by non-mixing dependent denitrification [M]
M_{DN}	Nitrate removed by mixing dependent denitrification [M]
N_{RE}	Nitrate removal efficiency [-]
M_{in}	Nitrate being introduced into streambed [M]

Abbreviations

HZ	Hyporheic zone
SW	Surface water
GW	Groundwater
HEF	Hyporheic exchange flow
MF	Mixing flux
NMD	Non-mixing dependent
MD	Mixing dependent
AR	Aerobic respiration
DN	Denitrification

Supporting information

Additional details of the model scenarios and model validation were displayed in the supporting information.

Data availability

All raw data can be provided by the first author upon request.

Competing interest

The authors declare that they have no conflict of interest.

Author contribution

Conceptualization: XP, YX

Formal analysis: XP

Funding acquisition: XP, ZW, YX, SK

Investigation: XP, ZW

Methodology: XP, ZW, YX

Writing-original draft: XP

Writing-review and editing: ZW, YX, MJ, SK

Project administration: ZW

Acknowledgments

The work was financially supported by the National Natural Science Foundation of China

Reference

Ahmerkamp, S., Winter, C., Janssen, F., Kuypers, M. M., and Holtappels, M.: The impact of bedform migration on benthic oxygen fluxes, J. Geophys. Res.: Biogeosci. 120, 2229–2242, https://doi.org/10.1002/2015JG003106, 2015.

Ahmerkamp, S., Winter, C., Krämer, K., Beer, D. D., Janssen, F., Friedrich, J., Kuypers, M. M. M., and Holtappels, M.: Regulation of benthic oxygen fluxes in permeable sediments of the coastal ocean, Limnol. Oceanogr. 62(5), 1935–1954, http://doi.org/10.1002/lno.10544, 2017.

Ascott, M. J., Stuart, M. E., Gooddy, D. C., Marchant, B. P., Talbot, J. C., Surridge, B. J., and Polya, D. A.: Provenance of drinking water revealed through compliance sampling, Environ. Sci.: Processes & Impacts, 21(6), 1052-1064, https://doi.org/10.1039/C8EM00437D, 2019.

Ashley, G. M.: Classification of large-scale subaqueous bedforms: A new look at an old problem-SEPM bedforms and bedding structures, J. Sediment. Res. 60(1), 160–172, https://doi.org/10.1306/212F9138-2B24-11D7-8648000102C1865D, 1990.

Azizian, M., Grant, S. B., Kessler, A. J., Cook, P. L. M., Rippy, M. A., and Stewardson, M. J.: Bedforms as biocatalytic filters: a pumping and streamline segregation model for nitrate removal in permeable sediments, Environ. Sci. Technol. 49, 10993–11002, https://doi.org/10.1021/acs.est.5b01941, 2015.

Bardini, L., Boano, F., Cardenas, M. B., Revelli, R., and Ridolfi, L.: Nutrient cycling in bedform induced hyporheic zones, Geochim. Cosmochim. Acta, 84, 47–61, https://doi.org/10.1016/j.gca.2012.01.025, 2012.

Bartholdy, J., Ernstsen, V. B., Flemming, B. W., Winter, C., Bartholomä, A., and Kroon, A.: On the formation of current ripples, Sci. Rep. 5(1), 11390, https://doi.org/10.1038/srep11390, 2015.

Bear, J., and Verruijt, A.: Modeling groundwater flow and pollution. D. Reidel Publishing Company, 1998.

Boano, F., Harvey, J. W., Marion, A., Packman, A. I., Revelli, R., Ridolfi, L., and Wörman, A.: Hyporheic flow and transport processes: Mechanisms, models, and biogeochemical implications, Rev. Geophys. 52, 603–679, https://doi.org/10.1002/2012RG000417, 2014.

Boano, F., Poggi, D., Revelli, R., and Ridolfi, L.: Gravity-driven water exchange between streams and hyporheic zones, Geophys. Res. Lett. 36, L20402, https://doi.org/10.1029/2009GL040147, 2009.

Boano, F., Revelli, R., and Ridolfi, L.: Water and solute exchange through flat streambeds induced by large turbulent eddies, J. Hydrol. 402, 290–296, https://doi.org/10.1016/j.jhydrol.2011.03.023, 2011.

1070 Boano, F., Revelli, R., and Ridolfi, L.: Modeling hyporheic exchange with unsteady stream

1071   discharge and bedform dynamics, Water Resour. Res. 49(7), 4089–4099,

1072   https://doi.org/10.1002/wrcr.20322, 2013.

1073 Bottacin-Busolin, A., and Marion, A.: Combined role of advective pumping and mechanical

1074   dispersion on time scales of bed form induced hyporheic exchange, Water Resour. Res. 46,

1075   W08518, https://doi.org/10.1029/2009WR008892, 2010.

1076 Boulton, A. J., Findlay, S., Marmonier, P., Stanley, E. H., and Valett, H. M.: The functional

1077   significance of the hyporheic zone in streams and rivers, Annu. Rev. Ecol. Syst. 29(1), 59–

1078   81, https://doi.org/10.1146/annurev.ecolsys.29.1.59, 1998.

1079 Briggs, M. A., Lautz, L. K., Hare, D. K., and González-Pinzón, R.: Relating hyporheic fluxes,

1080   residence times, and redox-sensitive biogeochemical processes upstream of beaver dams,

1081   Freshw. Sci. 32, 622–641, https://doi.org/10.1899/12-110.1, 2013.

1082 Burt, T. P., Howden, N. J. K., Worrall, F., Whelan, M. J., and Bieroza, M.: Nitrate in United

1083   Kingdom rivers: Policy and its outcomes since 1970, Environ. Sci. Technol., 45(1), 175–

1084   181, https://doi.org/10.1021/es101395s, 2011.

1085 Cardenas, M. B.: Hyporheic zone hydrologic science: A historical account of its emergence and

1086   a prospectus. Water Resour. Res. 51, 3601–3616, https://doi.org/10.1002/2015WR017028,

1087   2015.

1088 Cardenas, M. B., and Wilson, J. L.: The influence of ambient groundwater discharge on

1089   exchange zones induced by current-bedform interactions, J. Hydrol. 331, 103–109,

1090   https://doi.org/10.1016/j.jhydrol.2006.05.012, 2006.

Cardenas, M. B., Wilson, J. L., and Haggerty, R.: Residence time of bedform-driven hyporheic

exchange, Adv. Water Resour. 31(10), 1382–1386,

https://doi.org/10.1016/j.advwatres.2008.07.006, 2008.

Coleman, S. E., and Melville, B. W.: Bed-form development, J. Hydraul. Eng. 120(5), 544–560,

https://doi.org/10.1061/(ASCE)0733-9429(1994)120:5(544), 1994.

Conley, D. J., Paerl, H. W., Howarth, R. W., Boesch, D. F., Seitzinger, S. P., Havens, K. E.,

Lancelot, C., and Likens, G. E.: Ecology: controlling eutrophication: nitrogen and

phosphorus, Science 323, 1014–1015, https://doi.org/10.1126/science.1167755, 2009.

Dallmann, J., Phillips, C. B., Teitelbaum, Y., Sund, N., Schumer, R., Arnon, S., and Packman, A.

I.: Impacts of suspended clay particle deposition on sand-bed morphodynamics, Water

Resour. Res., 56(8), 2019WR027010, https://doi.org/10.1029/2019WR027010, 2020.

Drummond, J. D., Larsen, L. G., González-Pinzón, R., Packman, A. I., and Harvey, J. W.: Fine

particle retention within stream storage areas at base flow and in response to a storm event:

Particle retention stream storage areas, Water Resour. Res. 53, 5690–5705,

https://doi.org/10.1002/2016WR020202, 2017.

Elliott, A. H., and Brooks, N. H.: Transfer of nonsorbing solutes to a streambed with bed forms:

Theory, Water Resour. Res. 33(1), 123–136, https://doi.org/10.1029/96wr02784, 1997.

Fox, A., Boano, F., and Arnon, S.: Impact of losing and gaining streamflow conditions on hyporheic exchange fluxes induced by dune-shaped bed forms, Water Resour. Res. 50(3), 1895–1907, https://doi.org/10.1002/2013WR014668, 2014.

Fox, A., Packman, A. I., Boano, F., Phillips, C. B., and Arnon, S.: (2018). Interactions between suspended kaolinite deposition and hyporheic exchange flux under losing and gaining flow conditions, Geophys. Res. Lett., 45(9), 4077–4085. https://doi.org/10.1029/2018GL077951, 2018.

Gangi, A. F.: Permeability of unconsolidated sands and porous rocks. J. Geophys. Res. 90(B4), 3099–3104, https://doi.org/10.1029/JB090iB04p03099, 1985.

Gomez-Velez, J. D., Wilson, J. L., Cardenas, M. B., and Harvey, J. W.: Flow and residence times of dynamic river bank storage and sinuosity-driven hyporheic exchange, Water Resour. Res. 53, 8572–8595, https://doi.org/10.1002/2017WR021362, 2017.

Gomez-Velez, J. D., Harvey, J., Cardenas, M. B., and Kiel, B.: Denitrification in the Mississippi River network controlled by flow through river bedforms, Nat. Geosci. 8, 941–975, https://doi.org/10.1038/NGEO2567, 2015.

Gu, C., Hornberger, G. M., Herman, J. S., and Mills, A. L.: Effect of freshets on the flux of groundwater nitrate through streambed sediments, Water Resour. Res. 44, W05415, https://doi.org/10.1029/2007WR006488, 2008.

Harvey, J. W., Drummond, J. D., Martin, R. L., Mcphillips, L. E., Packman, A. I., Jerolmack, D.

    J., Stonedahl, S. H., Aubeneau, A. F., Sawyer, A. H., and Larsen, L. G.:

    Hydrogeomorphology of the hyporheic zone: Stream solute and fine particle interactions

    with a dynamic streambed, J. Geophys. Res. 117(G4), G00N11,

    https://doi.org/10.1029/2012JG002043, 2012.

Hedin, L. O., Von Fischer, J. C., Ostrom, N. E., Kennedy, B. P., Brown, M. G., and Robertson,

    G. P.: Thermodynamic constraints on nitrogen transformations and other biogeochemical

    processes at soil-stream interfaces, Ecology, 79(2), 684–703, https://doi.org/10.1890/0012-

    9658(1998)079[0684:TCONAO]2.0.CO;2, 1998.

Hester, E. T., Cardenas, M. B., Haggerty, R., and Sourabh, S. V. A.: The importance and

    challenge of hyporheic mixing, Water Resour. Res. 53, 3565–3575,

    https://doi.org/10.1002/2016WR020005, 2017.

Hester, E. T., Eastes, L. A., and Widdowson, M. A.: Effect of surface water stage fluctuation on

    mixing-dependent hyporheic denitrification in riverbed dunes, Water Resour. Res. 55,

    4668–4687, https://doi.org/10.1029/2018WR024198, 2019.

Hester, E. T., Young, K. I., and Widdowson, M. A.: Mixing of surface and groundwater induced

    by riverbed dunes: Implications for hyporheic zone definitions and pollutant reactions,

    Water Resour. Res. 49, 5221–5237, https://doi.org/10.1002/wrcr.20399, 2013.

Hester, E. T., Young, K. I., and Widdowson, M. A.: Controls on mixing-dependent

    denitrification in hyporheic zones induced by riverbed dunes: A steady state modeling

    study, Water Resour. Res. 50, 9048–9066, https://doi.org/10.1002/2014WR015424, 2014.

Howden, N. J. K., and Burt, T. P.: Temporal and spatial analysis of nitrate concentrations from

    the Frome and Piddle catchments in Dorset (UK) for water years 1978 to 2007: Evidence

    for nitrate breakthrough? Sci. Total Environ. 407(1), 507–526, http://doi.org/10.1016/j.

    scitotenv.2008.08.042, 2008.

Hu, H., Binley, A., Heppell, C. M., Lansdown, K., and Mao, X.: Impact of microforms on nitrate

    transport at the groundwater-surface water interface in gaining streams. Adv. Water Resour.

    73, 185–197, https://doi.org/10.1016/j.advwatres.2014.07.013, 2014.

Janssen, F., Cardenas, M. B., Sawyer, A. H., Dammrich, T., Krietsch, J., and de Beer, D.: A

    comparative experimental and multiphysics computational fluid dynamics study of coupled

    surface-subsurface flow in bed forms, Water Resour. Res. 48(8), W08514,

    https://doi.org/10.1029/2012WR011982, 2012.

Jiang, Q., Liu, D., Jin, G., Tang, H., Wei, Q., and Xu, J.: N2O dynamics in the hyporheic zone

    due to ripple migration, J. Hydrol. 610, 127891,

    https://doi.org/10.1016/j.jhydrol.2022.127891, 2022.

Kessler, A. J., Cardenas, M. B., and Cook, P. L. M.: The negligible effect of bed form migration

    on denitrification in hyporheic zones of permeable sediments, J. Geophys. Res.: Biogeosci.

    120, 538–548, https://doi.org/10.1002/2014JG002852, 2015.

Krause, S., Abbott, B. W., Baranov, V., Bernal, S., Blaen, P., Datry, T., Drummond, J., Fleckenstein, J. H., Velez, J. G., Hannah, D. M., Knapp, J. L. A., Kurz, M., Lewandowski, J., Martí, E., Mendoza-Lera, C., Milner, A., Packman, A., Pinay, G., Ward, A. S., and Zarnetzke, J. P.: Organizational principles of hyporheic exchange flow and biogeochemical cycling in river networks across scales, Water Resour. Res. 58 (3), 2021WR029771, https://doi.org/10.1029/2021WR029771, 2022.

Krause, S., Heathwaite, L., Binley, A., and Keenan, P.: Nitrate concentration changes at the groundwater-surface water interface of a small Cumbrian River, Hydrol. Processes, 23, 2195–2211, https://doi.org/10.1002/hyp.7213, 2009.

Krause, S., Tecklenburg, C., Munz, M., and Naden, E.: Streambed nitrogen cycling beyond the hyporheic zone: Flow controls on horizontal patterns and depth distribution of nitrate and dissolved oxygen in the upwelling groundwater of a lowland river, J. Geophys. Res.: Biogeosciences, 118, 54–67, https://doi.org/10.1029/2012JG002122, 2013.

Lansdown, K., Heppell, C. M., Dossena, M., Ullah, S., Heathwaite, A. L., Binley, A., Zhang, H., Trimmer, M., 2014. Fine-Scale in situ measurement of riverbed nitrate production and consumption in an armored permeable riverbed, Environ. Sci. Technol. 48 (8), 4425–4434, https://doi.org/10.1021/es4056005, 2014.

Lansdown, K., Heppell, C. M., Trimmer, M., Binley, A., Heathwaite, A. L., Byrne, P., and Zhang, H.: The interplay between transport and reaction rates as controls on nitrate attenuation in permeable, streambed sediments, J. Geophys. Res. Biogeosci. 120, 1093–1109, http://doi.org/10.1002/2014JG002874, 2015.

Lansdown, K., Trimmer, M., Heppell, C. M., Sgouridis, F., Ullah, S., Heathwaite, L., Binley, A., and Zhang, H.: Characterization of the key pathways of dissimilatory nitrate reduction and their response to complex organic substrates in hyporheic sediments, Limnol. Oceanogr. 57 (2), 387– 400, https://doi.org/10.4319/lo.2012.57.2.0387, 2012.

Lawrence, J. E., Skold, M. E., Hussain, F. A., Silverman, D. R., Resh, V. H., Sedlak, D. L., Luthy, R. G., and McCray, J. E.: Hyporheic zone in urban streams: A review and opportunities for enhancing water quality and improving aquatic habitat by active management, Environ. Eng. Sci. 30, 480–501, https://doi.org/10.1089/ees.2012.0235, 2013.

Liu, F., Ding, Y., Liu, J., Latif, J., Qin, J., Tian, S., Sun, S., Guan, B., Zhu, K., and Jia, H.: The effect of redox fluctuation on carbon mineralization in riparian soil: An analysis of the hotspot zone of reactive oxygen species production, Water Res. 265, 122294, https://doi.org/10.1016/j.watres.2024.122294, 2024.

Liu, Y., Liu, C., Nelson, W. C., Shi, L., Xu, F., Liu, Y., ... and Zachara, J. M.: Effect of water chemistry and hydrodynamics on nitrogen transformation activity and microbial community functional potential in hyporheic zone sediment columns, Environ. Sci. Technol., 51(9), 4877–4886, https://doi.org/10.1021/acs.est.6b05018, 2017.

Marzadri, A., Tonina, D., and Bellin, A.: Morphodynamic controls on redox conditions and on nitrogen dynamics within the hyporheic zone: application to gravel bed rivers with alternate-bar morphology, J. Geophys. Res.: Biogeosci. 117, 184–189, https://doi.org/10.1029/2012JG001966, 2012.

1208   Monod, J.: The growth of bacteria cultures, Annu. Rev. Microbiol., 3, 371–394,

1209   https://doi.org/10.1146/annurev.mi.03.100149.002103, 1949.

1210   Munz, M., Krause, S., Tecklenburg, C., and Binley, A.: Reducing monitoring gaps at the aquifer-

1211   river interface by modelling groundwater-surface water exchange flow patterns, Hydrol.

1212   Processes, 25, 3547–3562, https://doi.org/10.1002/hyp.8080, 2011.

1213   Naranjo, R. C., Niswonger, R. G., and Davis, C. J.: Mixing effects on nitrogen and oxygen

1214   concentrations and the relationship to mean residence time in a hyporheic zone of a riffle-

1215   pool sequence, Water Resour. Res. 51(9), 7202–7217,

1216   https://doi.org/10.1002/2014WR016593, 2015.

1217   Nogueira, G. E. H., Partington, D., Heidbuchel, I., and Fleckenstein, J. H.: Combined effects of

1218   geological heterogeneity and discharge events on groundwater and surface water mixing, J.

1219   Hydrol. 638, 131467, https://doi.org/10.1016/j.jhydrol.2024.131467, 2024.

1220   Nogueira, G. E. H., Schmidt, C., Brunner, P., Graeber, D., and Fleckenstein, J. H.: Transit-time

1221   and temperature control the spatial patterns of aerobic respiration and denitrification in the

1222   riparian zone, Water Resour. Res. 57 (12), 2021WR030117,

1223   https://doi.org/10.1029/2021WR030117, 2021.

1224   Nogueira, G. E. H., Schmidt, C., Partington, D., Brunner, P., and Fleckenstein, J. H.:

1225   Spatiotemporal variations in water sources and mixing spots in a riparian zone, Hydrol.

1226   Earth Syst. Sci, 26 (7), 1883–1905, https://doi.org/10.5194/hess-26-1883-2022, 2022.

Ocampo, C. J., Oldham, C. E., and Sivapalan, M.: Nitrate attenuation in agricultural catchments: shifting balances between transport and reaction, Water Resour. Res. 42(1), 85–88, https://doi.org/10.1029/2004WR003773, 2006.

Peleg, E., Teitelbaum, Y., and Arnon, S.: Exploring the influence of sediment motion on microplastic deposition in streambeds, Water Res. 249, 120952, https://doi.org/10.1016/j.watres.2023.120952, 2024.

Pescimoro, E., Boano, F., Sawyer, A. H., and Soltanian, M. R.: Modeling influence of sediment heterogeneity on nutrient cycling in streambeds, Water Resour. Res. 55, https://doi.org/10.1029/2018WR024221, 2019.

Ping, X., Xian, Y., and Jin, M.: Influence of bedform migration on nitrate reduction in hyporheic zones of heterogeneous sediments, Water Resour. Res. 58, e2022WR033258, https://doi.org/10.1029/2022WR033258, 2022.

Ping, X., Xian, Y., and Jin, M.: Effect of particulate organic carbon deposition on nitrate reduction in the hyporheic zone, Water Resour. Res. 59, e2022WR034253, https://doi.org/10.1029/2022WR034253, 2023.

Precht, E., Franke, U., Polerecky, L., and Huttel, M.: Oxygen dynamics in permeable sediments with wave-driven pore water exchange, Limnol. Oceanogr. 49(3), 693–705, https://doi.org/10.2307/3597786, 2004.

Quick, A. M., Reeder, W. J., Farrell, T. B., Tonina, D., Feris, K. P., and Benner, S. G.: Controls on nitrous oxide emissions from the hyporheic zones of streams, Environ. Sci. Technol. 50 (21), 11491–11500, https://doi.org/10.1021/acs.est.6b02680, 2016.

Raudkivi, A. J.: Ripples on stream bed, J. Hydraul. Eng. 123(1), 58–64,

    https://doi.org/10.1061/(ASCE)0733-9429(1997)123:1(58), 1997.

Reeder, W. J., Quick, A. M., Farrell, T. B., Benner, S. G., Feris, K. P., and Tonina, D.: Spatial

    and temporal dynamics of dissolved oxygen concentrations and bioactivity in the hyporheic

    zone, Water Resour. Res. 54, 2112–2128, https://doi.org/10.1002/2017WR021388, 2018.

Risse-Buhl, U., Arnon, S., Bar-Zeev, E., Oprei, A., Packman, A. I., Peralta-Maraver, I.,

    Robertson, A., Teitelbaum, Y., and Mutz, M.: Streambed migration frequency drives

    ecology and biogeochemistry across spatial scales, Wiley Interdiscip. Rev.: Water, 10.

    https://doi.org/10.1002/wat2.1632, 2023.

Rivett, M. O., Buss, S. R., Morgan, P., Smith, J. W. N., and Bemment, C. D.: Nitrate attenuation

    in groundwater: A review of biogeochemical controlling processes, Water Res. 42, 4215–

    4232, http://doi.org/10.1016/j.watres.2008.07.020, 2008.

Roche, K. R., Blois, G., Best, J. L., Christensen, K. T., Aubeneau, A. F., and Packman, A. I.:

    Turbulence links momentum and solute exchange in coarse-grained streambeds, Water

    Resour. Res. 54, 3225–3242, https://doi.org/10.1029/2017WR021992, 2018.

Roche, K. R., Li, A., Bolster, D., Wagner, G. J., and Packman, A. I.: Effects of turbulent

    hyporheic mixing on reach-scale transport, Water Resour. Res. 55,

    https://doi.org/10.1029/2018WR023421, 2019.

Rouse, J. D., Bishop, C. A., and Struger, J.: Nitrogen pollution: an assessment of its threat to

    amphibian survival, Environ. Health Perspect. 107, 799–803,

    https://doi.org/10.1289/ehp.99107799, 1999.

Salehin, M., Packman, A. I., and Paradis, M.: Hyporheic exchange with heterogeneous

streambeds: Laboratory experiments and modeling, Water Resour. Res., 40, W11504,

http://doi.org/10.1029/2003WR002567, 2004.

Santizo, K. Y., Widdowson, M. A., and Hester, E. T.: Abiotic mixing-dependent reaction in a

laboratory simulated hyporheic zone, Water Resour. Res. 56 (9), e2020WR027090,

https://doi.org/10.1029/2020WR027090, 2020.

Sawyer, A. H.: Enhanced removal of groundwater-borne nitrate in heterogeneous aquatic

sediments, Geophys. Res. Lett. 42(2), 403–410, https://doi.org/10.1002/2014GL062234,

2015.

Schindler, R. J., Parsons, D. R., Ye, L., Hope, J. A., Baas, J. H., Peakall, J., Manning, A. J.,

Aspden, A. J., Malarkey, J., and Simmons, S.: Sticky stuff: redefining bedform prediction

in modern and ancient environments, Geology, 43, 399–402,

https://doi.org/10.1130/G36262.1, 2015.

Schulz, H., Teitelbaum, Y., Lewandowski, J., Singer, G. A., and Arnon, S.: Moving bedforms

control CO2 production and distribution in sandy river sediments, J. Geophys. Res.:

Biogeosci. 128, e2022JG007156, https://doi.org/10.1029/2022JG007156, 2023.

Shelley, F., Klaar, M., Krause, S., and Trimmer, M.: Enhanced hyporheic exchange flow around

woody debris does not increase nitrate reduction in a sandy streambed, Biogeochem. 136

(3), 353-372, https://doi.org/10.1007/s10533-017-0401-2, 2017.

Soulsby, R.: Dynamics of marine sands: a manual for practical applications. Oceanogr. Lit. Rev.,

9, 947, 1997.

1290   Song, X., Chen, X., Stegen, J., Hammond, G., Song, H.-S., Dai, H., Graham, E., and Zachara, J.

1291   M.: Drought conditions maximize the impact of high-frequency flow variations on thermal

1292   regimes and biogeochemical function in the hyporheic zone, Water Resour. Res. 54 (10),

1293   7361–7382, https://doi.org/10.1029/2018WR022586, 2018.

1294   Stelzer, R. S., and Bartsch, L. A.: Nitrate removal in deep sediments of a nitrogen-rich river

1295   network: A test of a conceptual model, J. Geophys. Res. 117, G02027,

1296   http://doi.org/10.1029/2012JG001990, 2012.

1297   ~~Teitelbaum, Y., Shimony, T., Cifuentes, E. S., Dallmann, J., Phillips, C. B., Packman, A. I.,~~

1298   ~~Hansen, S. K., and Arnon, S.: A novel framework for simulating particle deposition with~~

1299   ~~moving bedforms, Geophys. Res. Lett. 49(4), e2021GL097223,~~

1300   ~~https://doi.org/10.1029/2021GL097223, 2022.~~

1301   Tonina, D., and Buffington, J. M.: Hyporheic exchange in gravel bed rivers with pool-riffle

1302   morphology: Laboratory experiments and three-dimensional modeling, Water Resour. Res.

1303   43, W01421, https://doi.org/10.1029/2005WR004328, 2007.

1304   Trauth, N., and Fleckenstein, J. H.: Single discharge events increase reactive efficiency of the

1305   hyporheic zone, Water Resour. Res. 53(1), 779–798.

1306   https://doi.org/10.1002/2016WR019488, 2017.

1307   Trauth, N., Musolff, A., Knller, K., Kaden, U. S., and Fleckenstein, J. H.: River water infiltration

1308   enhances denitrification efficiency in riparian groundwater, Water Resour. 130, 185–199,

1309   https://doi.org/10.1016/j.watres.2017.11.058, 2017.

Venditti, J. G., Church, M., and Bennett, S. J.: Morphodynamics of small-scale superimposed

    sand waves over migrating dune bed forms, Water Resour. Res., 41(10), W10423,

    https://doi.org/10.1029/2004WR003461, 2005.

Wolke, P., Teitelbaum, Y., Deng, C., Lewandowski, J., and Arnon, S.: Impact of bed form

    celerity on oxygen dynamics in the hyporheic zone, Water, 12(1), 62,

    https://doi.org/10.3390/w12010062, 2020.

Wondzell, S. M., LaNier, J., Haggerty, R., Woodsmith, R. D., and Edwards, R. T.: Changes in

    hyporheic exchange flow following experimental wood removal in a small, low-gradient

    stream, Water Resour. Res. 45, https://doi.org/10.1029/2008WR007214, 2009.

Woessner, W.: Stream and fluvial plain ground water interactions: rescaling hydrogeologic

    thought, Ground Water, 38(3), 15–25, https://doi.org/10.1111/j.1745-6584.2000.tb00228.x,

    2000.

Wu, L., Gomez-Velez, J. D., Li, L., and Carroll, K. C.: The fragility of bedform-induced

    hyporheic zones: Exploring impacts of dynamic groundwater table fluctuations, Water

    Resour. Res. 60, e2023WR036706, https://doi.org/10.1029/2023WR036706, 2024.

Xian, Y., Jin, M., Zhan, H., and Liang, X.: Permeable biofilms can support persistent hyporheic

    anoxic microzones, Geophys. Res. Lett. 49, e2021GL096948,

    https://doi.org/10.1029/2021GL096948, 2022.

Zarnetske, J. P., Haggerty, R., Wondzell, S. M., and Baker, M. A.: Dynamics of nitrate

    production and removal as a function of residence time in the hyporheic zone, J. Geophys.

    Res. Biogeosci. 116, G01025, https://doi.org/10.1029/2010JG001356, 2011a.

Zarnetske, J. P., Haggerty, R., Wondzell, S. M., and Baker, M. A.: Labile dissolved organic

carbon supply limits hyporheic denitrification, J. Geophys. Res. Biogeosci. 116, G04036,

https://doi.org/10.1029/2011JG001730, 2011b.

Zarnetske, J. P., Haggerty, R., Wondzell, S. M., Bokil, V. A., and González-Pinzón, R.: Coupled

transport and reaction kinetics control the nitrate source-sink function of hyporheic zones,

Water Resour. Res. 48 (11), 1–15, https://doi.org/10.1029/2012WR011894, 2012.

Zheng, L., Cardenas, M. B., Wang, L., and Mohrig, D.: Ripple effects: Bed form

morphodynamics cascading into hyporheic zone biogeochemistry, Water Resour. Res. 55,

7320–7342, https://doi.org/10.1029/2018WR023517, 2019.

Zhu, Y., Dai, H., and Yuan, S.: The competition between heterotrophic denitrification and

DNRA pathways in hyporheic zone and its impact on the fate of nitrate, J. Hydrol. 626:

130175, https://doi.org/10.1016/j.jhydrol.2023.130175, 2023.

Zomer, J. Y., and Hoitink, A. J. F.: Evidence of secondary bedform controls on river dune

migration, Geophys. Res. Lett. 51(15), https://doi.org/10.1029/2024GL109320, 2024.